Investigation of the Drivers of Sea Surface Salinity and North Atlantic Climate Variability Using a Stochastic Model

GLENN LIU,[a] YOUNG-OH KWON,[b] AND CLAUDE FRANKIGNOUL[b,c]

[a] *MIT-WHOI Joint Program in Oceanography, Applied Ocean Science and Engineering, Woods Hole, Massachusetts*
[b] *Woods Hole Oceanographic Institution, Woods Hole, Massachusetts*
[c] *LOCEAN, Sorbonne Université/IRD/CNRS/MNHN, Paris, France*

(Manuscript received 26 November 2024, in final form 20 June 2025, accepted 8 July 2025)

ABSTRACT: The role of ocean dynamics in Atlantic climate variability and predictability is often studied through the lens of sea surface temperature (SST). Unlike SST, sea surface salinity (SSS) is not directly damped by surface fluxes, and its low-frequency variability responds primarily to oceanic processes. This study investigates the drivers of SSS variability using a stochastic model hierarchy to disentangle oceanic and atmospheric contributions to Atlantic climate variability, in particular, the role of local vertical processes. Representation of SST and SSS persistence and variance is especially improved by the introduction of damping of anomalies below the mixed layer, though SSS anomalies remain too persistent. The effect of SST–evaporation feedback on SSS is comparatively smaller except in regions with strong SST–SSS correlation. Despite the lack of representation of geostrophic advection, the stochastic model successfully reproduces spatial patterns of recurring SST/SSS anomalies in the Community Earth System Model 1 (CESM1) Large Ensemble at monthly to interannual time scales. At multidecadal time scales, the stochastic model is unable to simulate the amplitude of SST/SSS variability, but their spatial patterns are broadly reproduced, suggesting that direct atmospheric forcing and local vertical processes are important for capturing these features. Further analysis of the processes missing from the stochastic model suggests that the lack of geostrophic advection is largely responsible for too persistent SSS in the stochastic model, while the lack of interannual mixed-layer depth variability explains the underestimated persistence and variance in some regions for both SST and SSS.

KEYWORDS: Atlantic Ocean; Ocean dynamics; Salinity; Stochastic models; Climate variability; Multidecadal variability

1. Introduction

Identification and prediction of the spatiotemporal signatures of multidecadal North Atlantic climate and its drivers have largely focused on anomalous sea surface temperatures (SSTs), but the relative roles of atmospheric and oceanic dynamics for Atlantic multidecadal variability (AMV, also Atlantic multidecadal oscillation) remain equivocal, despite its numerous impacts across the Earth system (see Zhang et al. 2019 and references therein). Less attention has been paid to multidecadal sea surface salinity (SSS) variability, in spite of its connections to drivers of AMV such as the North Atlantic Oscillation (NAO; Mignot and Frankignoul 2004; Frankignoul et al. 2009), low-frequency coherence with SST over the subpolar gyre (Zhang 2017; Friedman et al. 2017), and impacts on the Atlantic meridional overturning circulation (AMOC; Hughes and Weaver 1996; Patrizio et al. 2023). Furthermore, predicting and understanding SSS variability has societal relevance in itself; for example, extreme salinity anomalies can alter ocean circulation and low-frequency climate variability or serve as precursors to extreme weather events (Zhang and Vallis 2006; Oltmanns et al. 2024).

One possible pathway to understanding the drivers of SSS variability is through the stochastic climate model framework (Hasselmann 1976). This framework describes how rapidly varying atmospheric processes are communicated to the oceanic mixed layer through air–sea fluxes; these signals are integrated by the ocean due to its greater thermal inertia, resulting in a slowly varying climate response. The advantage of the stochastic model lies in its transparency and modularity, as individual processes can be successively added to understand its contributions. Applications have successfully captured both the spectra and persistence of midlatitude SST variability at locations across the North Atlantic and Pacific (Frankignoul and Hasselmann 1977; Frankignoul 1985; Hall and Manabe 1997; Deser et al. 2003; de Coëtlogon and Frankignoul 2003; Li et al. 2020; Patrizio and Thompson 2022; Liu et al. 2023).

While most studies focus on SST, only several have applied the stochastic model to investigating drivers of SSS variability. A key difference between the two variables is the absence of direct surface damping via air–sea fluxes for SSS, leading to unbounded growth of anomalies without other damping processes such as diffusion and advection (Spall 1993; Mignot and Frankignoul 2003; Zhang 2017). Subsequent studies have addressed the missing damping by adding a linear damping term to the stochastic SSS model. Hall and Manabe (1997) concluded that the local stochastic model failed to explain the low-frequency coherence between SST and SSS at North Atlantic ocean weather stations, suggesting that ocean circulation is important in these regions. Mignot and Frankignoul (2003) also found that anomalous Ekman advection is an important driver of interannual SSS variability and potentially more important than

Denotes content that is immediately available upon publication as open access.

Corresponding author: Glenn Liu, glennliu@mit.edu

DOI: 10.1175/JCLI-D-24-0694.1

local freshwater flux, particularly in regions influenced by large-scale atmospheric modes such as the NAO.

A common thread across these studies is a focus on competing contributions between atmospheric forcings (evaporation and precipitation) and horizontal ocean advection (often subsumed under the broad umbrella of "ocean dynamics"). The role of vertical entrainment and seasonality in SSS anomalies has received less attention, despite its ability to improve the representation of SST persistence and capture the AMV pattern in the stochastic framework (Liu et al. 2023).

A key process enabled by entrainment is reemergence: Anomalies from the previous winter remain insulated from interactions with the atmosphere under the seasonal summer thermocline and are reentrained as the mixed layer deepens again the subsequent fall, resulting in a winter-to-winter "memory" of anomalies (Alexander and Deser 1995). However, oceanic processes such as subduction, diffusion, and eddy mixing can erode thermocline anomalies before they reemerge, providing a source of damping for the deep anomalies that acts through entrainment (Park et al. 2006). These vertical processes impact both SST and SSS, but their contribution to low-frequency SSS variations remains unexplored. An investigation of these local processes and their impact on AMV is further warranted because strong reemergence requires a large seasonal mixed-layer depth (MLD) cycle—a condition fulfilled in the subpolar regions that have the longest persistence of SST and SSS anomalies (Timlin et al. 2002; Buckley et al. 2019). Despite data limitations, observed SSS reemergence in the North Atlantic hints at a third-year reemergence signal in SSS, but not SST, consistent with the lack of surface damping of the former (Frankignoul et al. 2021). However, long-term observational data for SSS are scarce; thus, analysis of SSS anomalies in model output with good spatiotemporal coverage may provide further insight into the driving processes.

To investigate how reemergence and other local dynamics contribute to SSS behavior and its implications for North Atlantic climate, we develop a hierarchy of stochastic models. The model parameters are estimated using thousands of years of output from the Community Earth System Model 1 (CESM1) Large Ensemble, allowing us to isolate contributions from specific processes to answer the following:

1) What regions have strong SSS reemergence, and how does this compare with SST?
2) What are the physical processes that drive SSS variability and persistence at these locations?
3) Can the stochastic model capture the pattern and amplitude of multidecadal SST and SSS variability, and what are the implications for our understanding of AMV?

This paper is structured as follows: We describe the CESM1 output and patterns of North Atlantic SST/SSS reemergence (sections 2 and 3). To understand the processes that generate such patterns, we introduce the stochastic model and estimates of the required parameters (sections 4a,b). Using a hierarchy, we isolate contributions from damping of subsurface anomalies and SST–evaporation feedback on SSS at representative locations, and broaden our analysis to the basinwide patterns of multidecadal SST/SSS variability (sections 4c,d). We identify regions of large discrepancies with CESM1, discuss potential contributions of key processes missing from the stochastic model (section 5), and then summarize our results (section 6).

2. CESM1

Limited observational records complicate understanding of the drivers and statistics of multidecadal North Atlantic climate. We thus focus on understanding the behavior of SST and SSS variability in CESM1, with land, ice, atmosphere, and ocean components at nominally 1° horizontal resolution (Hurrell et al. 2013). We use monthly mean output from the historical period (1920–2005) of the 42-member large ensemble simulations, providing 3612 years of output (Kay et al. 2015). Since our objective is to disentangle contributions of specific processes in internal North Atlantic climate variability rather than the impact of external forcings, large ensembles facilitate the isolation of the internal component by subtracting the ensemble mean (Deser et al. 2020). Furthermore, focusing on a single model provides an opportunity to understand the dynamics within a physically consistent system, avoiding confounding factors from intermodel biases.

Prior to all calculations, the mean seasonal cycle and ensemble mean are removed at each location and time step. Oceanic outputs are regridded to the atmospheric grid using bilinear interpolation. To focus on ocean–atmosphere interactions, we exclude grid points where the sea ice fraction exceeds 5% at any time during the simulations (cyan line, Fig. 1).

It is critical to note that the coarse resolution of CESM1 impacts the representation of SSS and SST, particularly through underestimating contributions from mesoscale ocean processes (Kirtman et al. 2012; Small et al. 2020). The coarse resolution also biases the position of the Gulf Stream and North Atlantic Current, altering the locations of strong SST/SSS gradients and the regions where advective processes may play a critical role. Furthermore, the North Atlantic in CESM1 is saltier than observations, impacting AMOC strength and the contributions of nonlocal processes to low-frequency SST/SSS variability (Danabasoglu et al. 2012; Patrizio et al. 2023).

3. Patterns of SST and SSS Reemergence

To identify regions in the North Atlantic where local vertical processes are important for setting the memory of anomalies, we use the reemergence index (REI; Alexander and Deser 1995; Byju et al. 2018), derived from the monthly lagged autocorrelation function using the difference between the winter maximum and the preceding summer minimum autocorrelation (AC):

$$\mathrm{REI} = \max(\mathrm{AC}_{\mathrm{winter}}) - \min(\mathrm{AC}_{\mathrm{summer}}), \tag{1}$$

where the minima and maxima are located around lags of 6 and 12 months, respectively, with a search tolerance of ±3 months. The REI is calculated at each grid point using monthly autocorrelation functions for February or March anomalies, when the

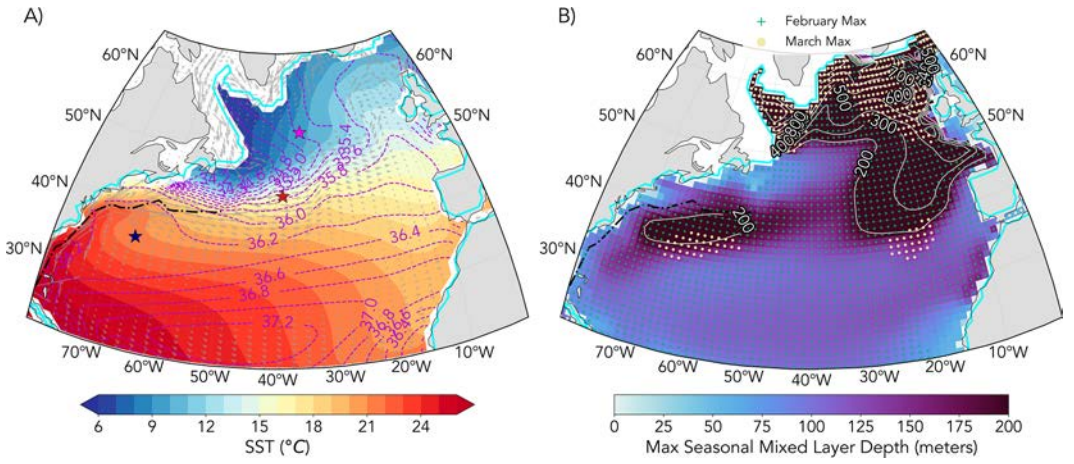

FIG. 1. (a) Ensemble-mean surface currents (vectors) over the mean SST (colors) and SSS (contours) in CESM1. (b) Maximum MLD of the mean seasonal cycle in CESM1. MLDs deeper than 200 m are contoured every 100 m (white). The Xs (dots) denote a maximum MLD in February (March). The extent of the ice mask used for our simulations (cyan line) and the Gulf Stream's mean position (black line), given by the local maxima in surface current speed, are indicated in both panels and included for reference in figures hereafter.

MLD is deepest at most extratropical locations (Fig. 1b; Hanawa and Sugimoto 2004).

The REI patterns in CESM1 for SST (Fig. 2a) and SSS (Fig. 2c) share many features, including maximum values in the far northeastern subpolar gyre (55°–60°N), a secondary maximum in the Sargasso Sea just south of the Gulf Stream, and a tongue of elevated values connecting both regions along the North Atlantic Current.

The strongest SSS reemergence signals occur where wintertime MLDs are deep, just south of the maximum sea ice extent and within the Labrador Sea (Fig. 2c). While the locations of SST REI maxima coincide generally with regions of deep wintertime MLDs (Fig. 1b), this correspondence is limited. For example, the SST REI maximum is located southeast of Greenland near the Irminger Sea rather than in the Labrador Sea, where MLDs are deeper (Figs. 1b and 2a).

4. The stochastic salinity model

a. Theory and formulation

To understand how specific physical processes impact SSS and SST variability and shape the reemergence patterns in CESM1, we apply the stochastic climate model framework (Hasselmann 1976; Frankignoul and Hasselmann 1977). Its simplicity is a key advantage, permitting transparent investigation of how individual processes, such as vertical entrainment and subsurface damping, generate key features of SST and SSS behavior.

Assuming homogeneous density, horizontal velocities, and salinity within the mixed layer, the vertically integrated salinity equation in the open ocean can be expressed as (Frankignoul 1985; Frankignoul et al. 1998)

$$h\frac{\partial S}{\partial t} = \frac{\overline{S}}{\rho}(E - P) - (h\mathbf{u})\cdot\nabla_{\mathrm{H}}S - (S - S_d)w_e + \kappa_{\mathrm{H}}h\nabla^2 S + \kappa_z\frac{\partial S_d}{\partial z}. \tag{2}$$

The right-hand side terms represent evaporation (E) and precipitation (P) forcing, advection of horizontal salinity gradients (∇_{H}) by lateral mixed-layer currents ($h\mathbf{u}$), vertical entrainment (w_e) of anomalies below the mixed layer (S_d), parameterized horizontal mixing with a constant diffusivity (κ_{H}), and parameterized vertical mixing at the mixed-layer base with a turbulent diffusivity (κ_z; see Table A1 of appendix A for a full list of parameters). The w_e consists of both local MLD changes and the divergence of horizontal currents and is only active when positive:

$$w_e = \frac{\partial h}{\partial t} + \nabla_{\mathrm{H}}\cdot(h\mathbf{u}). \tag{3}$$

Following Frankignoul (1985), the SSS anomaly equation is obtained by decomposing the terms into monthly climatological means ($\overline{\ }$) and deviations ($'$):

$$\begin{aligned}\frac{\partial S'}{\partial t} = {} & \underbrace{\frac{\overline{S}}{\rho\overline{h}}(E' - P')}_{\mathrm{A}} - \underbrace{\frac{(h\mathbf{u})'\cdot\nabla_{\mathrm{H}}(\overline{S} + S')}{\overline{h}}}_{\mathrm{B}} - \underbrace{\frac{\overline{(h\mathbf{u})}\cdot\nabla_{\mathrm{H}}S'}{\overline{h}}}_{\mathrm{C}} \\ & - \underbrace{\frac{h'}{\overline{h}}\frac{\partial\overline{S}}{\partial t}}_{\mathrm{D}} - \underbrace{\frac{(S' - S'_d)}{\overline{h}}\overline{w_e}}_{\mathrm{E}} - \underbrace{\frac{\overline{S} + S' - \overline{S_d} - S'_d}{\overline{h}}w'_e}_{\mathrm{F}} \\ & + \underbrace{\kappa_{\mathrm{H}}\nabla^2 S' + \frac{h'}{\overline{h}}\kappa_{\mathrm{H}}\nabla^2(\overline{S} + S')}_{\mathrm{G}} + \underbrace{\frac{1}{\overline{h}}\kappa_z\frac{\partial S'_d}{\partial z}}_{\mathrm{H}}.\end{aligned} \tag{4}$$

The right-hand-side terms are

A: Anomalous evaporation (E') and precipitation (P') forcing with a nominal density (ρ = 1026 kg m^{-3}), mean salinity ($\overline{S}$), and MLD ($\overline{h}$).
B: Anomalous advection (u') of horizontal salinity gradients.
C: Mean advection ($\overline{u}$) of anomalous salinity gradients.
D: Changes due to MLD variability (h').
E: Mean entrainment of salinity anomalies beneath the mixed layer.

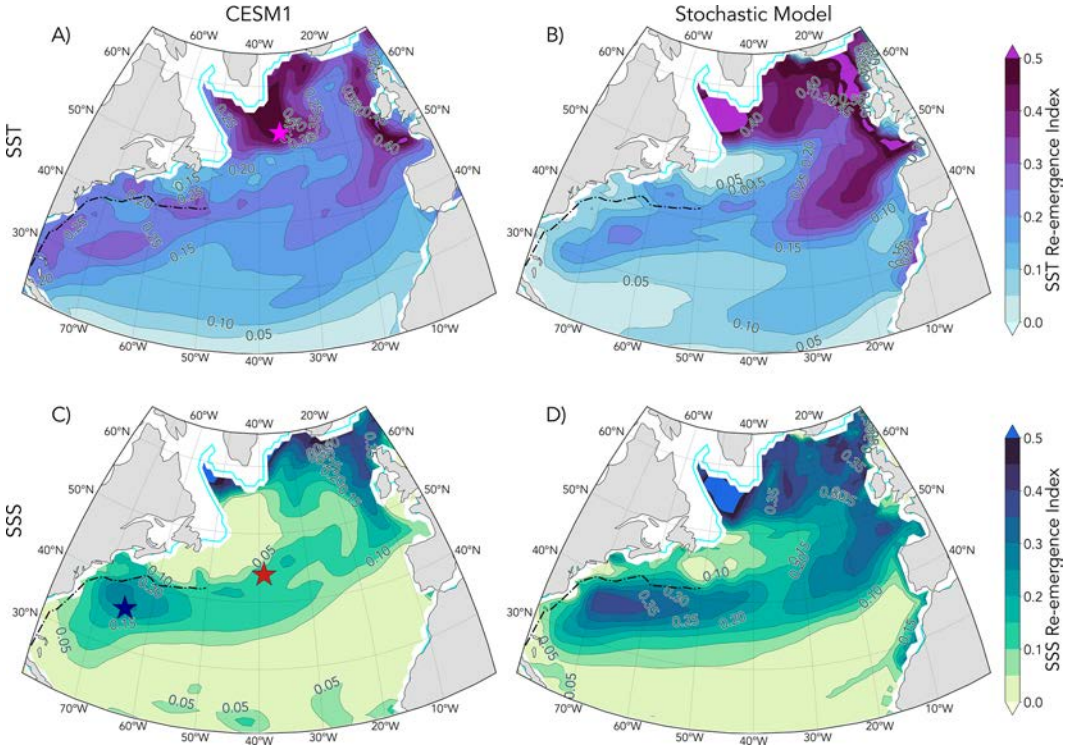

FIG. 2. REIs for wintertime anomalies of (a),(b) SST and (c),(d) SSS in (left) CESM1 and (right) the stochastic model. The ensemble-average pattern for CESM1 is shown. (c) The Sargasso Sea (blue star), (c) North Atlantic Current (red star), and (a) Irminger Sea (magenta star) locations are indicated.

F: Anomalous entrainment acting upon the salinity jump across the mixed-layer base.
G: Horizontal mixing and eddy stirring.
H: Vertical diffusion at the mixed-layer base.

The horizontal currents (terms B and C) and their divergence in Eq. (3) are further decomposed into geostrophic and Ekman components ($u = u_{geo} + u_{ek}$). Since geostrophic currents are largely forced by remote processes such as Rossby waves and mesoscale eddies, the latter of which is not resolved by CESM1, they cannot be simulated by the local stochastic model. We thus retain only the advection of mean gradients by anomalous Ekman currents driven by local wind stress (Frankignoul 1985). Since the mean Ekman advection is neglected, w_e is now:

$$\overline{w_e} = \frac{\partial \overline{h}}{\partial t}, \; w_e' = \frac{\partial h'}{\partial t} + \nabla_H \cdot (h\mathbf{u}_{ek})'. \tag{5}$$

Our current formulation does not include an energy equation that allows for estimating h' and w_e' from wind and buoyancy forcing, so we neglect terms D and F. Contributions of anomalous Ekman pumping to w_e' are neglected as they are smaller than wind mixing (Sterl and Hazeleger 2003) and are found to be less important than horizontal Ekman convergence where Ekman forcing is important for SST (Haarsma et al. 2005); comparison of these two components in CESM1 verifies previous results, with local wind mixing ($\partial h'/\partial t$) greater than anomalous Ekman pumping at all grid points in the North Atlantic (not shown).

The mixing term G encapsulates multiple processes including stirring by mesoscale and submesoscale eddies, providing a potential source of ocean damping (Bryan and Bachman 2015; Laurindo et al. 2024). Since our objective is to investigate specific processes such as subsurface damping and entrainment rather than to exhaustively include all parameterizations present in CESM1, we drop this term to prioritize transparency within the simple stochastic model framework (Frankignoul 1985; Danabasoglu et al. 2012). Since our model does not provide the vertical structure of salinity or temperature under the mixed layer, we neglect the diffusive flux at the mixed-layer base (term H). Potential contributions from some of the neglected terms are discussed in sections 5 and 6.

These simplifications leave three primary processes: 1) evaporation–precipitation forcing, 2) advection of the mean salinity gradients by anomalous Ekman currents, and 3) mean vertical entrainment:

$$\frac{\partial S'}{\partial t} = \frac{\overline{S}}{\rho \overline{h}}(E' - P') - \frac{(h\mathbf{u}_{ek})' \cdot \nabla(\overline{S})}{\overline{h}} - \frac{(\overline{w_e})}{\overline{h}}(S' - S_d'). \tag{6}$$

To consider potential connections to SST, we substitute anomalous evaporation (E') with the downward latent heat flux ($Q_L' = -LE'$), where L is the specific heat of evaporation (2.5×10^6 J kg^{-1}).

A key assumption of the stochastic model is the time-scale separation between rapidly varying "weather" forcing and the slowly varying "climate" response produced by the ocean. We

apply this separation to decompose Q'_L into stochastic (F'_L) and temperature-dependent ($\lambda^L T'$) components (Frankignoul et al. 1998; Frankignoul and Kestenare 2002):

$$Q'_L = F'_L - \lambda^L T'. \tag{7}$$

We can then rewrite Eq. (6) as (hereafter $\overline{h} = h$, as we only consider the mean seasonal cycle of MLD)

$$\frac{\partial S'}{\partial t} = \frac{\overline{S}}{\rho h L}(-F'_L + \lambda^L T') - \frac{\overline{S}}{\rho h} P' - \frac{\overline{w_e}}{h}(S' - S'_d) + Q'_{\mathrm{ek},S}, \tag{8}$$

where anomalous Ekman forcing is given by $Q'_{\mathrm{ek},S} = -[(h\mathbf{u}_{\mathrm{ek}})' \cdot \nabla \overline{S}]/\overline{h}$.

We introduce the SST–evaporation feedback (λ^e) representing an SSS change induced by the latent heat flux from an SST anomaly (Hughes and Weaver 1996; Frankignoul et al. 1998):

$$\lambda^e = \frac{\overline{S}}{\rho h L}\lambda^L. \tag{9}$$

Previous studies have speculated that this term, while small on interannual time scales, could contribute to SSS variability on decadal and longer time scales. This addition results in a simplified stochastic model for salinity:

$$\frac{\partial S'}{\partial t} = \lambda^e T' + \frac{\overline{S}}{\rho h}\left(-\frac{F'_L}{L} - P'\right) - \frac{\overline{w_e}}{h}(S' - S'_d) + Q'_{\mathrm{ek},S}. \tag{10}$$

To compute T' in the SST–evaporation feedback term, we build upon the corresponding SST stochastic model (Liu et al. 2023) with the addition of forcing by anomalous Ekman currents $Q'_{\mathrm{ek},T}$:

$$\frac{\partial T'}{\partial t} = -\frac{\lambda^N}{\rho c_p h} T' + \frac{F'_N}{\rho C_p h} - \frac{\overline{w_e}}{h}(T' - T'_d) + Q'_{\mathrm{ek},T}. \tag{11}$$

Note that T' is forced by the stochastic component (F'_N) of the net heat flux (Q'_N, positive downward) independent of T':

$$F'_N = Q'_N + \lambda^N T', \tag{12}$$

where λ^N is the net surface heat flux feedback.

To integrate the stochastic model, we discretize Eqs. (10) and (11) using the forward method, as outlined in appendix B. The final discretized form of the salinity stochastic model is given by

$$S'(t + \Delta t) = e^{-\lambda \Delta t} S'(t) + \left\{\frac{1}{\Delta t}\ln\left[\frac{h(t + \Delta t)}{h(t)}\right]\overline{S'_d} + \left[\frac{\overline{S}}{\rho h}\left(\frac{F_{L'}}{L} - P'\right)\right] + Q'_{\mathrm{ek},S} + \lambda^e T'\right\}\left(\frac{1 - e^{-\lambda \Delta t}}{\lambda}\right). \tag{13}$$

The total damping of the system is represented by λ. Importantly, entrainment is the only source of damping directly applied to SSS ($\lambda = \overline{w_e}/h$), occurring only when the mixed layer deepens. This is in contrast to SST that experiences both heat-flux and entrainment damping [$\lambda = \lambda^N + (\overline{w_e}/h)$].

b. Parameter estimation

Unless otherwise stated, all estimates are performed pointwise, separately for each CESM1 ensemble member and month. The estimates are then averaged across all ensemble members for the final stochastic model inputs.

1) Heat flux and SST–evaporation feedbacks

We estimate the heat flux feedbacks by taking the monthly lagged covariance of Eq. (7) with T' (Frankignoul et al. 1998; Frankignoul and Kestenare 2002; Park et al. 2005; Liu et al. 2023). By definition, the stochastic component F'_L vanishes when S' or T' leads, leaving the latent heat flux feedback (λ^L):

$$\lambda^L = -\frac{\mathrm{cov}[Q'_L(t),\ T'(t - \tau)]}{\mathrm{cov}[T'(t),\ T'(t - \tau)]}, \tag{14}$$

where τ is taken to be 1 month. The λ^N is similarly estimated by substituting Q'_L with Q'_N. The feedback is set to zero at locations where either the numerator or denominator of Eq. (14) is not significant at the 95% confidence level, using a two-sided t test (Park et al. 2005). Seasonally averaged λ^N estimates (colors) and their corresponding e-folding time scales (τ^N; contours) are shown, where the latter is estimated by converting λ^N from units of W m^{-2} °C^{-1} to months, where $\tau^N = \rho C_p h \Delta t (\lambda^N)^{-1}$ (Fig. 3).

The λ^N is strongest along the western boundary due to enhanced turbulent heat fluxes when cold continental air is advected over the warm Gulf Stream (Figs. 3a–d). This translates to short τ^N (<6 months), in agreement with previous estimates (Frankignoul and Kestenare 2002; Park et al. 2005). In contrast, regions with the longest τ^N are in the far northern subpolar gyre due to comparatively weak λ^N and deep MLDs (Figs. 3a–d). Insignificant λ^N estimates occur near the maximum extent of sea ice in the northeastern subpolar gyre (Figs. 3a,b). As expected, regions of strong λ^L over the subtropics also have large λ^e, particularly during summer and fall with shallower MLDs (Figs. 3g,h).

2) Stochastic forcings

From Eq. (13), the total stochastic forcing amplitude of SSS by local atmospheric variability is the sum of the stochastic latent heat flux (F'_L), precipitation (P'), and Ekman forcings ($Q'_{\mathrm{ek},S}$). Similarly, the total forcing for the stochastic temperature equation includes stochastic net heat flux (F'_N) and Ekman forcing ($Q'_{\mathrm{ek},T}$). To understand relationships between local drivers of SSS/SST and large-scale North Atlantic climate such as the AMV, it is important to preserve both the *amplitude* and *spatial coherence* of each individual forcing. We accomplish this by first constructing an empirical orthogonal function (EOF)-based F'_N forcing and then establishing associated patterns of other forcing terms, so that the temporal and spatial coherence between the

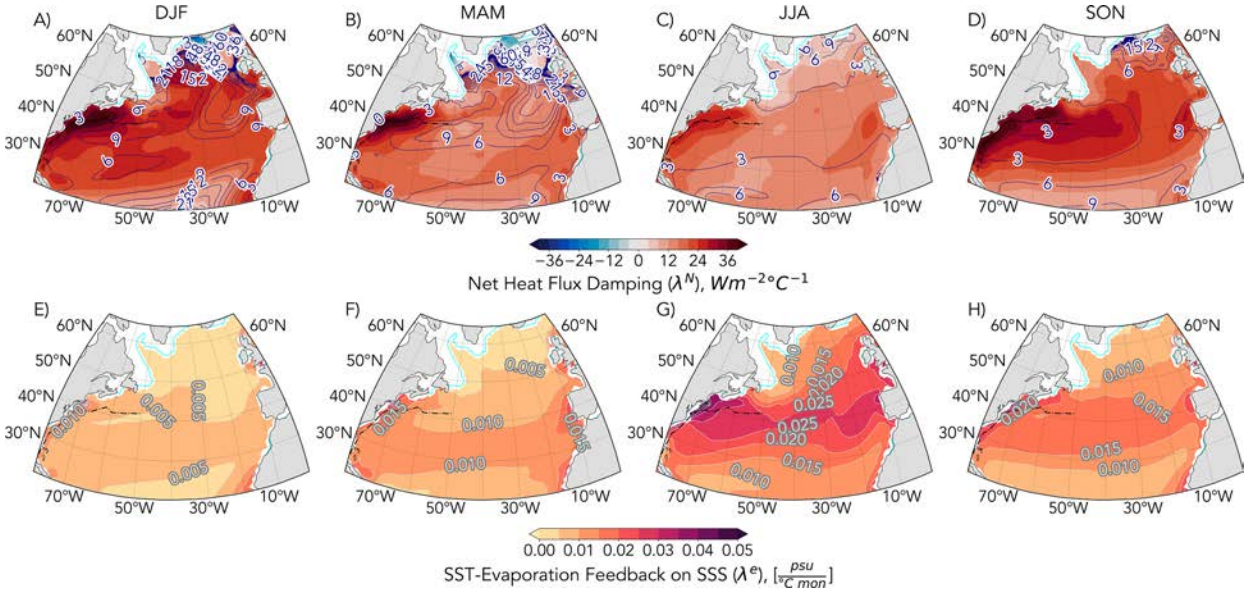

FIG. 3. (a)–(d) Seasonally averaged damping time scales in months (τ^N; contours) due to net heat flux feedback (λ^N; color). (e)–(h) Seasonally averaged SST–evaporation feedback on SSS (λ^e).

various forcings are retained (Liu et al. 2023). The details of this procedure are described in appendix C.

EOF 1 of the wintertime F'_N resembles heat flux patterns associated with positive NAO, where increased westerly winds over the subpolar gyre lead to greater heat loss (Fig. 4a) and increased evaporation and precipitation with opposing effects on salinity (Figs. 4c,d; Hurrell and Deser 2010). The second mode resembles the east Atlantic pattern, where increased low pressure over the center of the subpolar gyre leads to anomalous counterclockwise circulation, strengthening the westerlies and intensifying the heat loss over the North Atlantic Current (Msadek and Frankignoul 2009). These patterns are largely consistent with the enhanced evaporation and precipitation forcing (third and fourth columns).

To compute the Ekman forcing, the anomalous zonal and meridional wind stress (τ'_x, τ'_y) are regressed to F'_N EOFs (step 3 of appendix C) and used to compute the associated horizontal Ekman currents:

$$\langle u'_{\mathrm{ek}}, v'_{\mathrm{ek}} \rangle = \frac{1}{\rho h f} \langle \tau'_y, -\tau'_x \rangle, \tag{15}$$

where f is the Coriolis parameter. These currents are then used to advect the mean SST or SSS gradients computed using a centered difference, for instance:

$$Q'_{\mathrm{ek},S} = u'_{\mathrm{ek}} \frac{\partial \overline{S}}{\partial x} + v'_{\mathrm{ek}} \frac{\partial \overline{S}}{\partial y}. \tag{16}$$

The patterns are similar between both variables. The $Q'_{\mathrm{ek},T}$ has comparable amplitude to F'_N near the region of largest gradients between the subpolar and subtropical gyres (Figs. 4k,l), while $Q'_{\mathrm{ek},S}$ is more comparable to the stochastic E and P forcing.

3) DAMPING OF SUBSURFACE ANOMALIES

Previous stochastic model formulations often assume that subsurface temperature (T'_d) and salinity anomalies (S'_d) remain constant until reentrainment into the mixed layer the following fall and winter. However, these anomalies may be impacted by local and nonlocal processes while detrained, including subduction, obduction, diffusion, eddy mixing, and lateral subsurface advection (de Coëtlogon and Frankignoul 2003; Sugimoto and Hanawa 2005, 2007; Liu and Huang 2012). Park et al. (2006) parameterized these processes as a fixed "effective diffusivity," applying an exponential decay to subsurface anomalies of 10^{-8} s^{-1} (e-folding time scale of approximately 38.6 months), derived from subsurface temperatures at locations across the North Pacific.

We build upon this approach by explicitly estimating pointwise values of "subsurface memory" (λ^d), representing the bulk effect of ocean processes on damping subsurface anomalies (S'_d, T'_d). S'_d entrained into the mixed layer [Eq. (10)] is given by

$$S'_d = \lambda^d_S S'_{d0}, \tag{17}$$

where S'_{d0} is the SSS at the time of detrainment. The λ^d has a value between 0 and 1, where larger λ^d indicates weaker damping, translating to longer persistence of subsurface anomalies. The T'_d is given by the same expression but with λ^d_T estimated separately.

The λ^d is quantified using correlations between subsurface anomalies from vertical profiles of S' and T' in CESM1. For illustration, we provide an example of the procedure at 50°N, 30°W (Fig. 5):

1) For a given month when entrainment is occurring, identify the depth from which the anomaly was detrained earlier

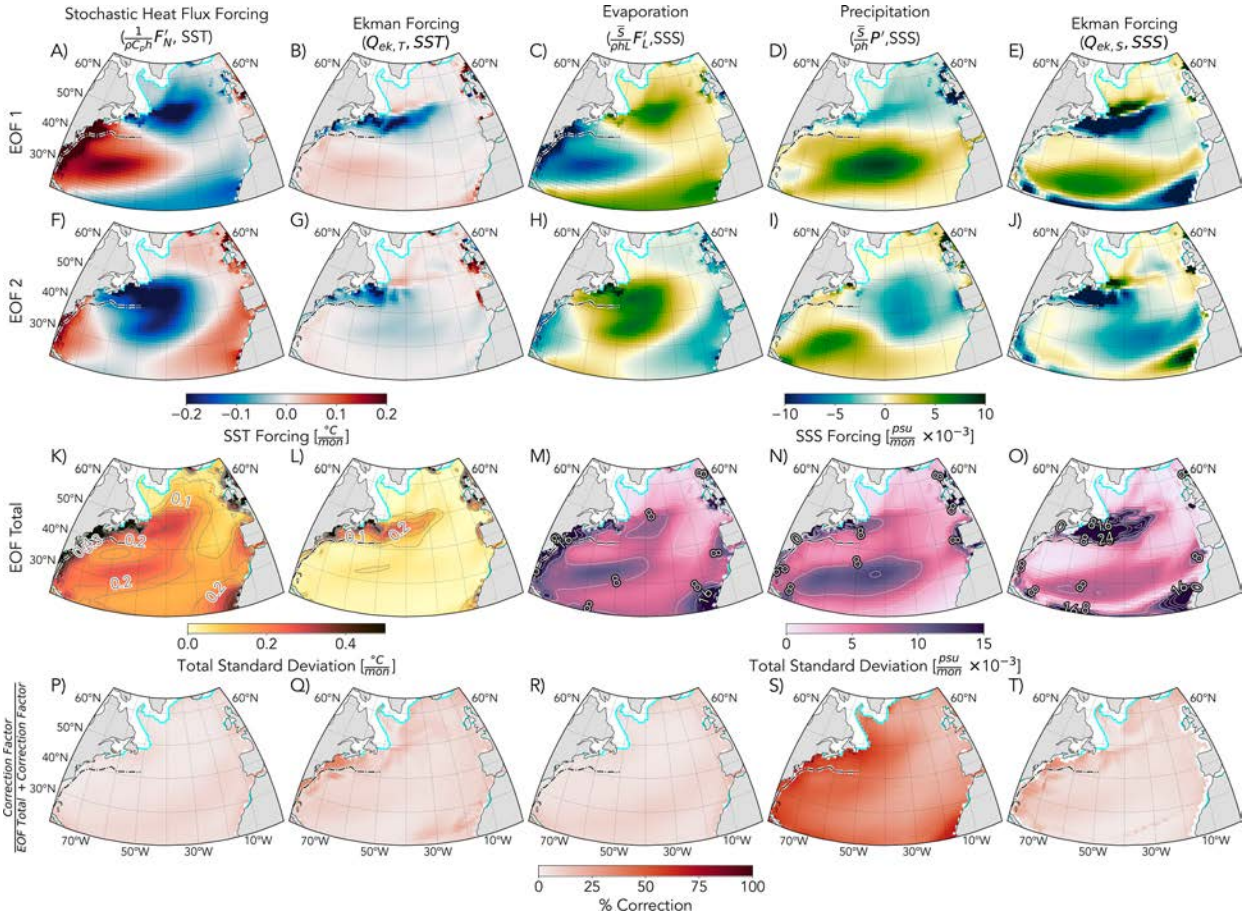

FIG. 4. Mean wintertime (February/March) forcing terms for (left two columns) SST and (right three columns) SSS stochastic models. (a)–(e) EOF 1 and (f)–(j) EOF 2 are shown for illustration, as well as the total amplitude of the EOF forcing summed across all retained modes (k)–(o). The local correction factor (percentage relative to the EOF total plus correction) for each term is shown at the bottom (p)–(t).

based on the climatological MLD annual cycle at the location. For example, anomalies entrained in October were detrained between April (68.7 m) and May (31.7 m), or at the averaged depth of 50.2 m.

2) Find the vertical model level (55 m) nearest to the detrainment depth and extract the time series of temperature and salinity anomalies.
3) Compute λ_T^d and λ_S^d as the correlation between anomalies at the month of detrainment and anomalies 1 month before entrainment. We take anomalies 1 month prior because anomalies at the month of entrainment are already within the mixed layer and influenced by atmospheric forcing, leading to overestimated subsurface damping. Hence, λ^d for anomalies entrained in October is given by the correlation between April and September anomalies at the depth of 55 m.

To visualize the persistence of subsurface anomalies (Fig. 6), we assume an exponential decay ($\lambda^d = e^{-\Delta t/\tau^d}$) to recover the subsurface memory time scale (τ^d) of subsurface anomalies:

$$\tau_S^d = \frac{-\Delta t}{\ln(\lambda_S^d)}, \tag{18}$$

where Δt is the number of months between detrainment and entrainment. As expected, shorter time scales are common throughout the North Atlantic in summer (Figs. 6a,d), when the MLD is shallow and more likely to be influenced by perturbations such as mechanical mixing (Alexander and Penland 1996). Time scales increase toward fall and winter as anomalies are drawn from deeper depths that should be less affected by surface processes. Subsurface anomalies have short τ^d along the Gulf Stream and North Atlantic Current, particularly for SST, suggesting that they may be advected away or damped by nonlocal ocean processes.

While the spatial patterns and seasonal variation of temperature and salinity subsurface memory are similar, S'_d is overall more persistent. Notable regions of long (60+ month) T'_d persistence are found southeast of Greenland near the Irminger Sea and in the eastern subtropics around 40°N between winter and early spring (Figs. 6b,c). The τ_S^d is

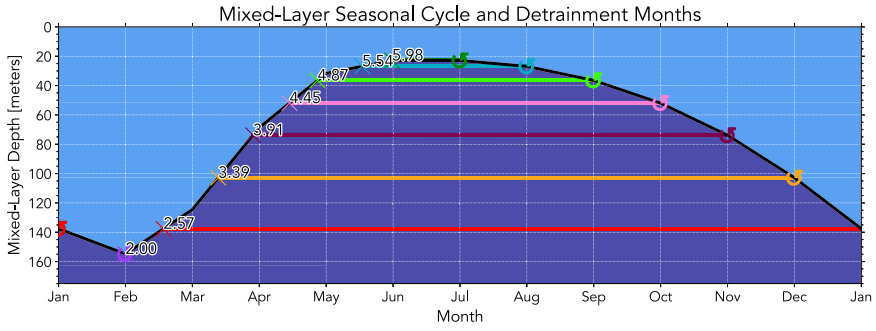

FIG. 5. Schematic depicting the entrainment mechanism applied in the stochastic model at a location with a typical MLD seasonal cycle in the subpolar gyre (50°N, 30°W). Circular arrows denote the entrainment month and depth, while "x" denotes the corresponding detrainment time, with the value indicated in fractional months.

slightly larger in late summer and fall, with an elevated tongue of persistent subsurface anomalies (>30–50 months) extending diagonally south of the North Atlantic Current, roughly corresponding to the region of deeper MLDs (Fig. 1), subduction, and North Atlantic subtropical mode water formation (Liu and Huang 2012). The presence of a thick, uniform water mass could lead to reduced vertical gradients of temperature and salinity, reducing processes such as mixing and diffusion that would damp subsurface anomalies. Overall, regions of long subsurface memory coincide with regions of strong REI, suggesting the importance of this parameter for reemergence strength and persistence.

c. *Applying the stochastic model hierarchy*

The stochastic model is integrated for 10 000 years at a monthly time step, separately at each point in the North Atlantic (80°W–0°, 20°–60°N). The mean annual cycle in MLD over the historical period of CESM1 (h) is used in our integrations. Regions equatorward of 20°N are excluded due to longer time scales of atmospheric persistence, violating the time-scale separation in stochastic model theory (Hasselmann 1976). We also exclude points within 1° of the coastline to focus on direct forcing of SST/SSS rather than the effects of upwelling, downwelling, or continental runoff (Alexander and Scott 2008).

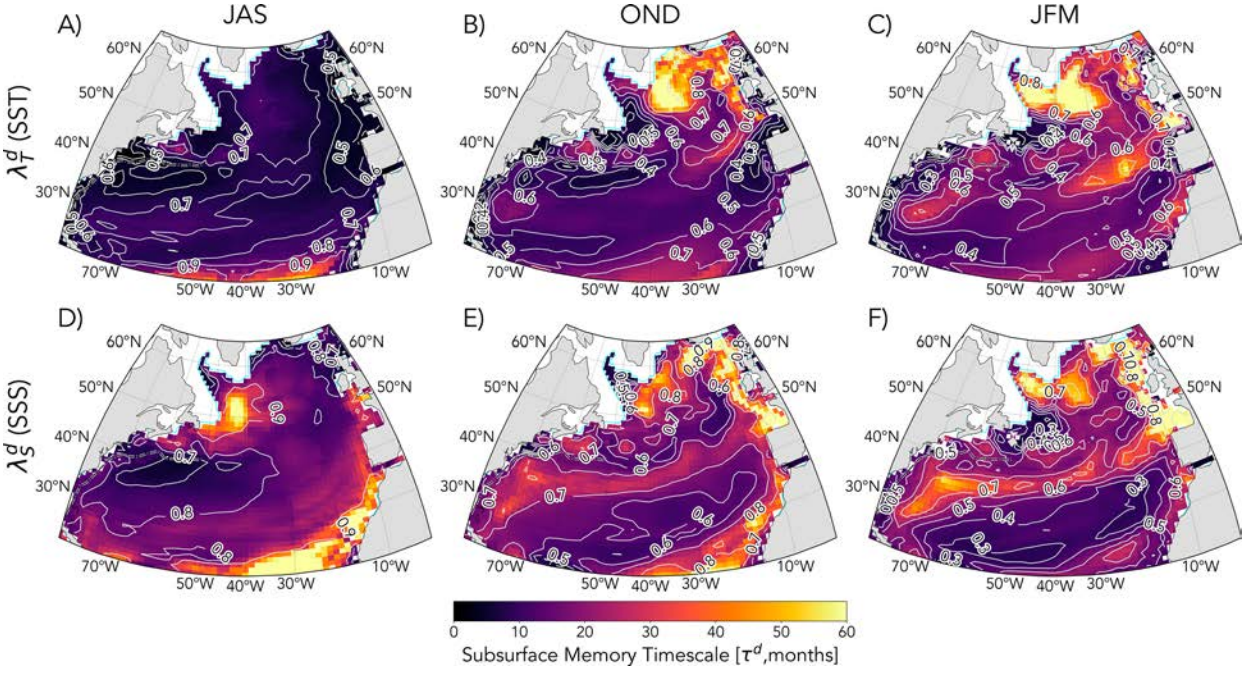

FIG. 6. The e-folding time scale of deep anomalies entrained at a given month, averaged over (left) late summer, (center) fall, and (right) winter for (a)–(c) SST and (d)–(f) SSS. Light gray contours show the corresponding correlation between the detrained and entrained anomalies, or the subsurface damping parameter λ^d.

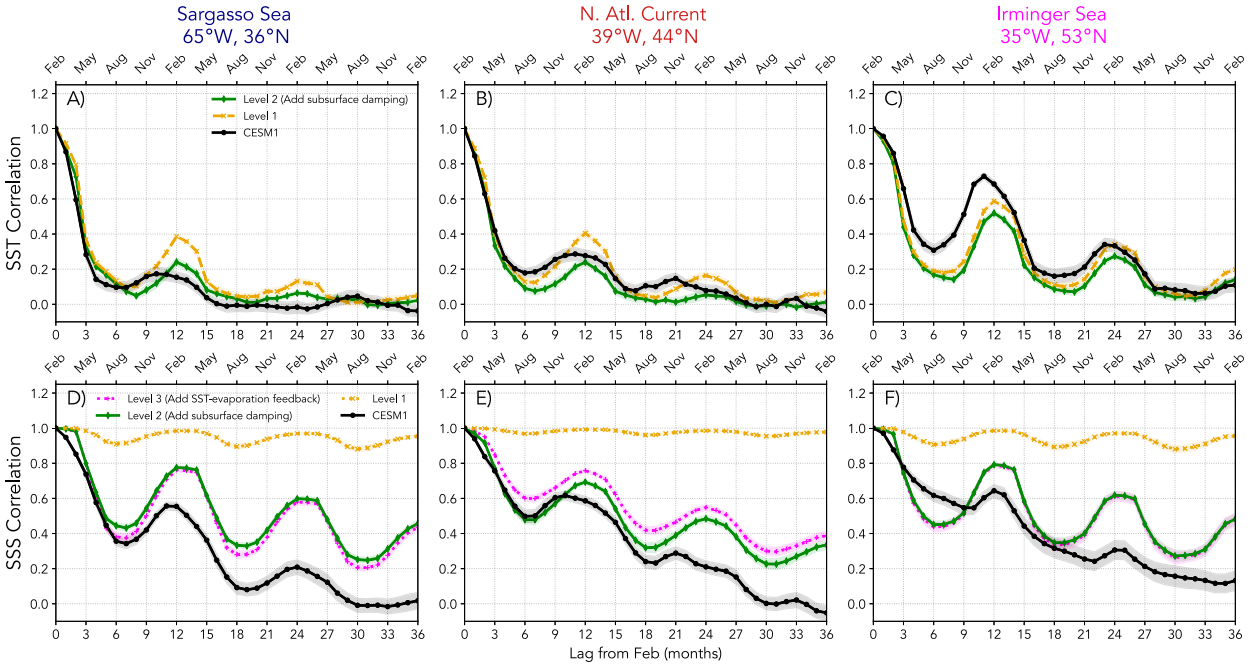

FIG. 7. Persistence of wintertime (February) anomalies quantified through the monthly lagged autocorrelation functions for (a)–(c) SST and (d)–(f) SSS at selected locations with strong reemergence. The corresponding metric for CESM1 is shown in black. Shading indicates one standard error across the 42 ensemble members (CESM1) or ten 1000-yr chunks (stochastic model). Compare the effect of adding detrainment damping (gold to green) and adding SST–evaporation feedback on SSS (green to magenta).

Despite its simplified representation of vertical entrainment, the stochastic model remarkably captures major features of the REI amplitude and patterns in CESM1 for both SST and SSS, emphasizing that the persistence and its seasonal progression are reasonably reproduced, even without horizontal ocean dynamics (Figs. 2b,d).

To investigate how specific processes impact SST and SSS behavior and generate the REI pattern, we build a stochastic model hierarchy by iteratively including specific parameters. Beginning with the stochastic model with entrainment and Ekman forcing [level 1 (without subsurface damping)], we first consider the effect of adding subsurface damping (level 2). For SSS, we further investigate the contribution of SST–evaporation feedback (level 3). All cases are then compared to CESM1 with full ocean physics to elucidate potential contributions from the absent processes. The stochastic model is integrated at each hierarchy level using identical sets of forcings to maximize comparability across experiments.

We focus on three representative locations (Fig. 2, stars) in 1) the Sargasso (SAR) Sea, 2) North Atlantic Current (NAC), and 3) the Irminger (IRM) Sea. These locations were selected because they have strong SST/SSS reemergence signals and are away from coastlines and sea ice, criteria that reflect a balance between our two objectives: 1) understanding the role of reemergence in SST/SSS variability and 2) choosing locations where the local stochastic model is well suited to explain variability. While both IRM and SAR are away from regions of strong advection (Fig. 1), NAC is characterized by large SST/SSS gradients and relatively strong advection (Buckley et al. 2014, 2015). Comparisons with NAC allow for investigating drivers of strong SST/SSS reemergence in both near-advective and nonadvective regimes. We extend the comparisons throughout the North Atlantic in section 5a.

1) Damping of subsurface anomalies

We first examine the wintertime persistence using the February autocorrelation function. Despite its simplicity, the stochastic model captures the approximate timing of SST wintertime reemergence peaks, but in SAR and NAC, the peaks are overestimated without subsurface damping (level 1, gold line). This peak is better reproduced when subsurface damping is added (level 2, green line), translating to comparable REI values between the stochastic model and CESM1 (Figs. 7a,b). This stresses the importance of subsurface damping for accurately capturing the amplitude of SST reemergence. However, SST persistence in the initial summer and fall (lags 1–24) is underestimated in IRM irrespective of subsurface damping, suggesting that the missing dynamics should provide additional SST persistence (Fig. 7c).

The effect of subsurface damping is more striking for SSS, where its absence leads to highly unrealistic persistence at all locations (Figs. 7d–f, gold line). With subsurface damping (green line), the persistence of SSS is strongly reduced, although not sufficiently. Due to the unrealistic persistence of SSS without subsurface damping, we will not consider SSS results without subsurface damping any further.

Next, we investigate how subsurface damping impacts interannual variance (σ^2_{Int}) for each month (de Coëtlogon and

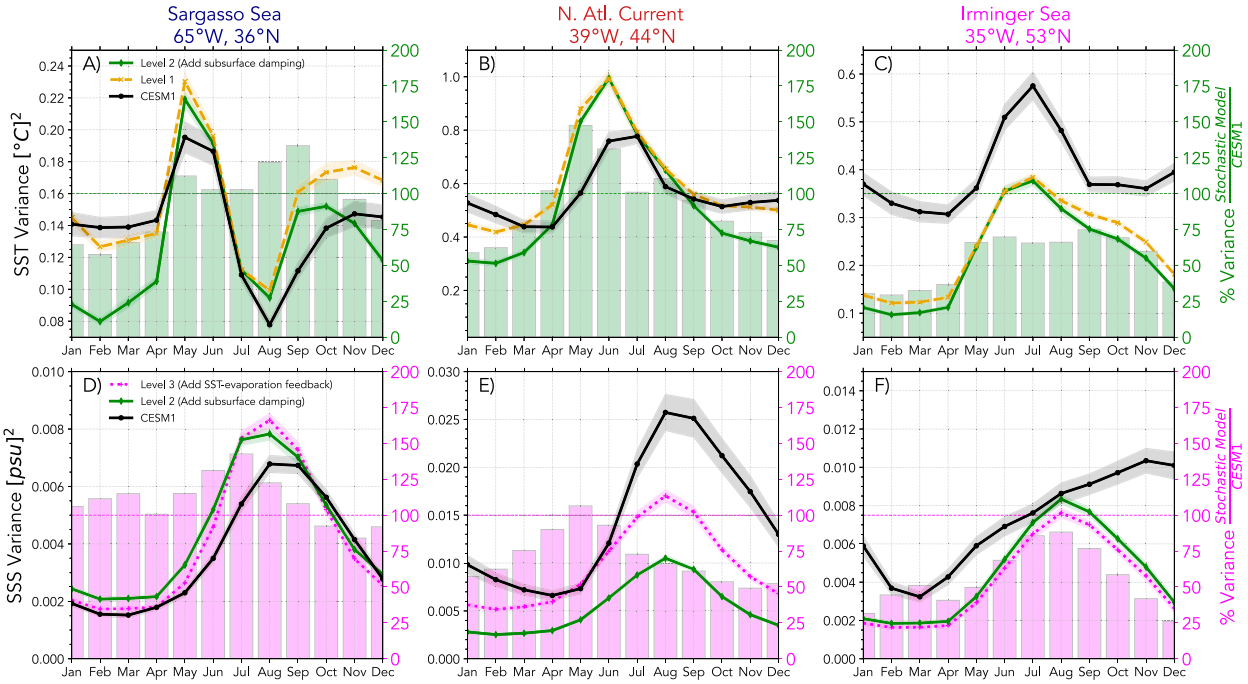

FIG. 8. Interannual (a)–(c) SST and (d)–(f) SSS variance for each month, where each subplot column corresponds to one of the selected locations. The color conventions for the lines and shadings are identical to Fig. 7. Note the difference in *y*-axis scale between subplots. Green and pink bars indicate the percentage of variance explained by the most complex stochastic model (i.e., level 2 for SST, level 3 for SSS) relative to CESM1, while the dashed horizontal line indicates the 100% level.

Frankignoul 2003; Gozdz et al. 2024). The σ^2_{Int}(SST) in CESM1 is generally higher in the summer months as the shallower MLDs translate to smaller heat capacity (Figs. 8a,c, black lines). The stochastic model captures this behavior; subsurface damping reduces variance during the late fall and wintertime when entrainment is active, somewhat decreasing the correspondence with CESM1. However in SAR, minimum σ^2_{Int}(SST) occurs instead in August (Fig. 8a) due to the offset between seasonal minima in stochastic heat flux forcing and MLD (not shown).

Unlike for SST, maximum values of σ^2_{int}(SSS) occur in early fall due to timing of seasonal maxima in precipitation and Ekman forcing for SAR and NAC, respectively (Figs. 8d–f, black lines). The addition of subsurface damping (Figs. 8d–f, green lines) allows the stochastic model to capture σ^2_{int}(SSS), but not at IRM, where the maximum occurs instead in late fall. This feature is shared by surrounding points and corresponds to a region of shallower wintertime mixed-layer depths extending into the Irminger Sea, though the mechanism is not clear from our model and requires further investigation (Fig. 1). Without subsurface damping, SSS variances are overestimated by an order of magnitude across all locations and months with little seasonal variation (not shown).

Subsurface damping reduces both SST and SSS power primarily at low frequencies, resulting in location-dependent differences with CESM1. In SAR, the SST power spectra are well captured, suggesting that the atmospherically forced regime of the stochastic model is appropriate (Fig. 9a). In contrast, SSS remains overestimated at low frequencies, highlighting the need for additional damping from the missing processes (Figs. 9d,e). In NAC, while SST power is underestimated at low frequencies (<10 years^{-1}), the largest discrepancies for SSS are underestimates around subdecadal (5–10 year) periods, suggesting that the missing processes, especially horizontal advection, may have frequency-dependent impacts that differ between each variable (Figs. 9b,e). Both SST and SSS power are underestimated relative to CESM1 in IRM, suggesting the importance of the missing ocean dynamics there for enhancing variability, especially for SST at low frequencies (Figs. 9c,f).

2) THE SST–EVAPORATION FEEDBACK ON SSS

When SST and SSS are positively correlated, SST–evaporation feedback should enhance the variance and persistence of SSS, as positive SST anomalies would increase the evaporation which leads to enhanced positive SSS anomalies and vice versa [Eq. (10)]. In CESM1, strong positive correlations occur along the NAC and within the IRM and Labrador Seas (Fig. 10a). In contrast, weakly positive SST–SSS correlations occur in the western subtropics and central subpolar gyre (Fig. 10). Negative correlations along the western subtropics may be due to the climatological position of the salinity maximum in 20°–30°N (Fig. 1), leading to opposing meridional gradients of salinity and temperature south of its location. Northward mean advection along the Gulf Stream brings fresher and warmer anomalies from the equator, producing negative correlations.

Overall, the stochastic model reproduces strong positive correlations along the NAC and far northeastern subpolar

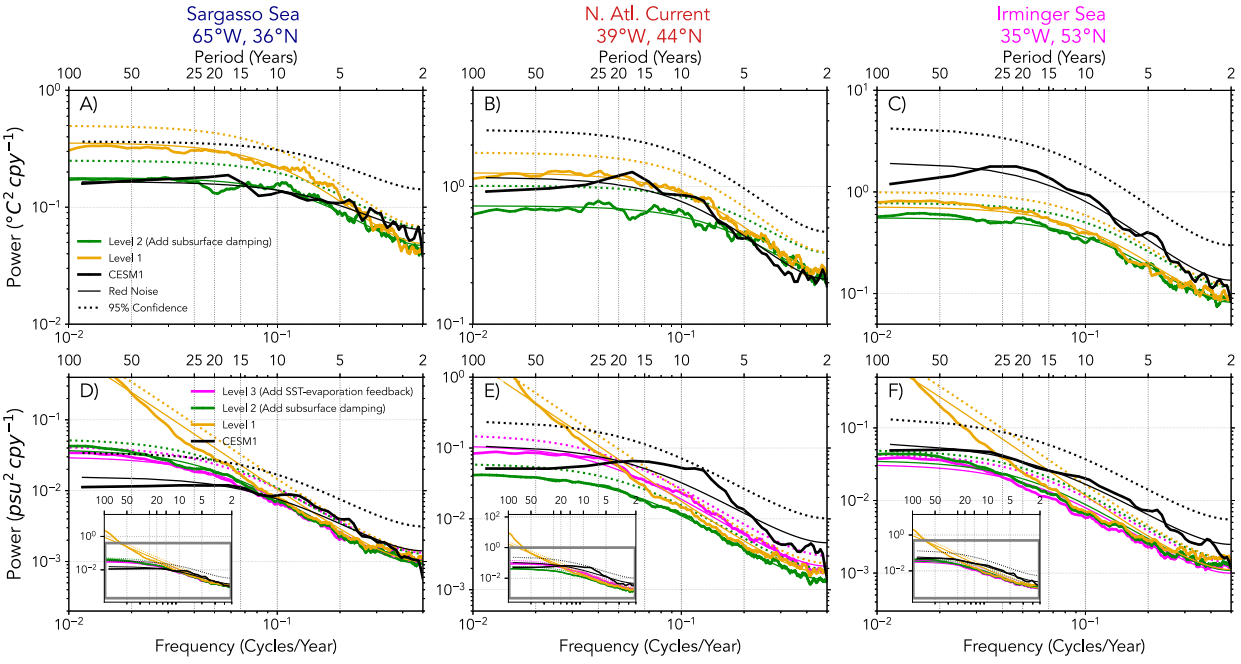

FIG. 9. Power spectra for the corresponding points for (a)–(c) SST and (d)–(f) SSS. Solid thin (dotted) lines indicate the red-noise null hypothesis (95% significance level). CESM1 (stochastic model) spectra were smoothed across 2 (20) adjacent bands using a modified Daniell window. The color conventions for the lines are identical to previous figures. Note the difference in *y*-axis limits between subplots.

gyre in CESM1. The positive values along the NAC are collocated with regions of large SST/SSS gradients (Fig. 1) and Ekman forcing (Figs. 4l,o), suggesting its potential role in driving the CESM1 correlation pattern. Ekman forcing in SSS drives a sharp, unrealistic dipole of positive–negative correlations northwest of Africa in the stochastic model, where the meridional salinity gradient is positive, opposing the mean temperature gradient.

The SST–evaporation feedback on the SSS has limited effects on SSS persistence and variance except over the NAC region, where SST and SSS are positively correlated. The addition of this feedback leads to a slight increase in persistence (Fig. 7e, green versus magenta) and an increase in SSS variance across all months (Fig. 8e) and frequencies (Fig. 9e). However, this further increases the already too large SSS persistence and translates to overestimated power relative to CESM1 at lower frequencies.

d. *Patterns of multidecadal SST and SSS variability*

Expanding beyond the representative locations, we investigate if stochastic model reproduces basinwide AMV patterns

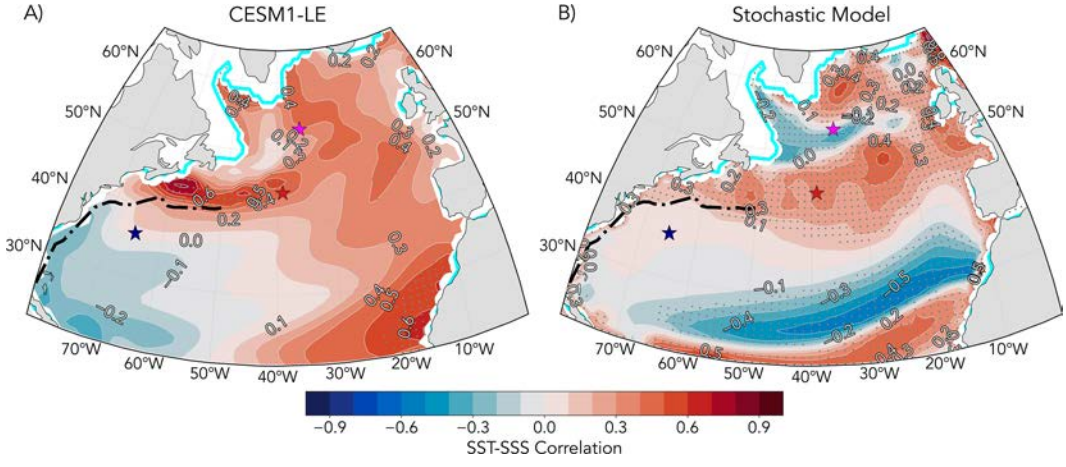

FIG. 10. Correlation between SST and SSS anomalies in (a) CESM1 and (b) the stochastic model. The illustrative locations are indicated by stars. Stippling indicates significant correlation at the 5% level, determined by simulating 10 000 pairs of red-noise time series with the same lag-1 correlation as SST/SSS at each location.

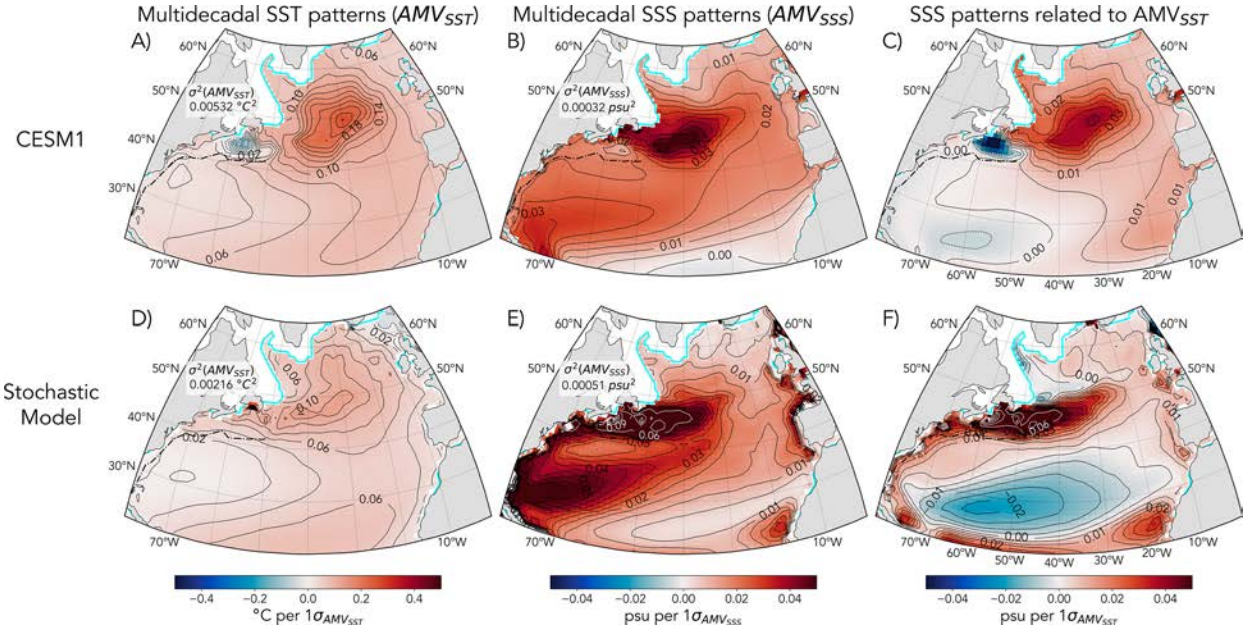

FIG. 11. (a),(d) The AMV pattern for SST (°C per $\sigma_{AMV,SST}$) and (b),(e) SSS (psu per $\sigma_{AMV,SSS}$), and (c)–(f) SSS regressed to SST AMV (psu per $\sigma_{AMV,SST}$) in (top) CESM1 and (bottom) the stochastic model. The variance for the SST and SSS AMV indices is shown within the corresponding subplots.

comparable to CESM1. We compute AMV indices for both SST and SSS as the 10-year low-pass-filtered, area-weighted average of each respective anomalies between 20 and 60°N, 80°W–0° (Liu et al. 2023). These indices are standardized and used to obtain the AMV regression patterns for SST and SSS (Fig. 11).

The stochastic model successfully simulates major features of multidecadal SST and SSS patterns in CESM1 (Fig. 11). The centers of action in the subpolar gyre (for SST) and the North Atlantic current (for SSS) are well reproduced, highlighting the importance of local forcing and damping for capturing multidecadal patterns of SST and SSS variability. This is consistent with previous findings (Liu et al. 2023) that the stochastic model can largely recreate the SST AMV pattern once the spatial coherences of the stochastic forcing are realistic, albeit with an underestimated amplitude. Note that while additions of Ekman forcing and subsurface damping yield more comparable variances along the Gulf Stream–NAC region (60°–70°W, 40°–50°N) than in Liu et al. (2023), the amplitude of the SST AMV index remains underestimated by more than 50%, leaving a substantial role for the missing processes to enhance low-frequency SST variance (Figs. 11a,d). In contrast, the multidecadal low-frequency SSS variability in the North Atlantic is overestimated by nearly 1.5 times (Figs. 11b,e), consistent with the overestimated SSS persistence; this again emphasizes the importance of missing damping for capturing SSS behavior at low frequencies.

It is also of interest to regress SSS anomalies onto the SST AMV index to recover the SSS pattern associated with the traditional SST AMV. In contrast with the dominant pattern of low-frequency SSS variability, a prominent dipole of SSS anomalies appears in CESM1, with negative (positive) values south of Newfoundland (in the eastern subpolar region; Fig. 11c). This pattern closely resembles the SST AMV, where co-occurrence of warm and salty (cool and fresh) anomalies suggests the influence of advection. The dipole highlights contrasting behavior between the subpolar and subtropical regions of the North Atlantic: The former exhibits coherent multidecadal SST and SSS variability, while the relationship is more ambiguous over the subtropical latitudes (Zhang 2017). This SSS dipole pattern is absent in the stochastic model, replaced by large and positive values along the entirety of the North Atlantic Current (Fig. 11f), likely due to anomalous Ekman forcing acting upon meridional gradients of SST and SSS of the same sign (Fig. 1). Overall, this suggests that additional lateral processes, such as geostrophic advection, are needed to correctly simulate the relationship between SST and SSS at multidecadal time scales. This contrasts the multidecadal pattern of SSS alone that is well captured by the stochastic model.

5. Discussion of contributions from missing processes

a. Where do the missing ocean dynamics play a role?

We identify where dynamics missing from the stochastic model affect SST/SSS persistence and standard deviation (σ), by calculating pointwise differences between CESM1 and the most complex stochastic models (level 2 for SST and level 3 for SSS). Contributions to persistence are quantified by differences (stochastic model minus CESM1) in the wintertime autocorrelation averaged over two lag intervals: 1) the initial decorrelation over spring and summer (lags 1 to 6, Figs. 12a,c) and 2) the reemergence peak between fall and winter (lags 6 to 18,

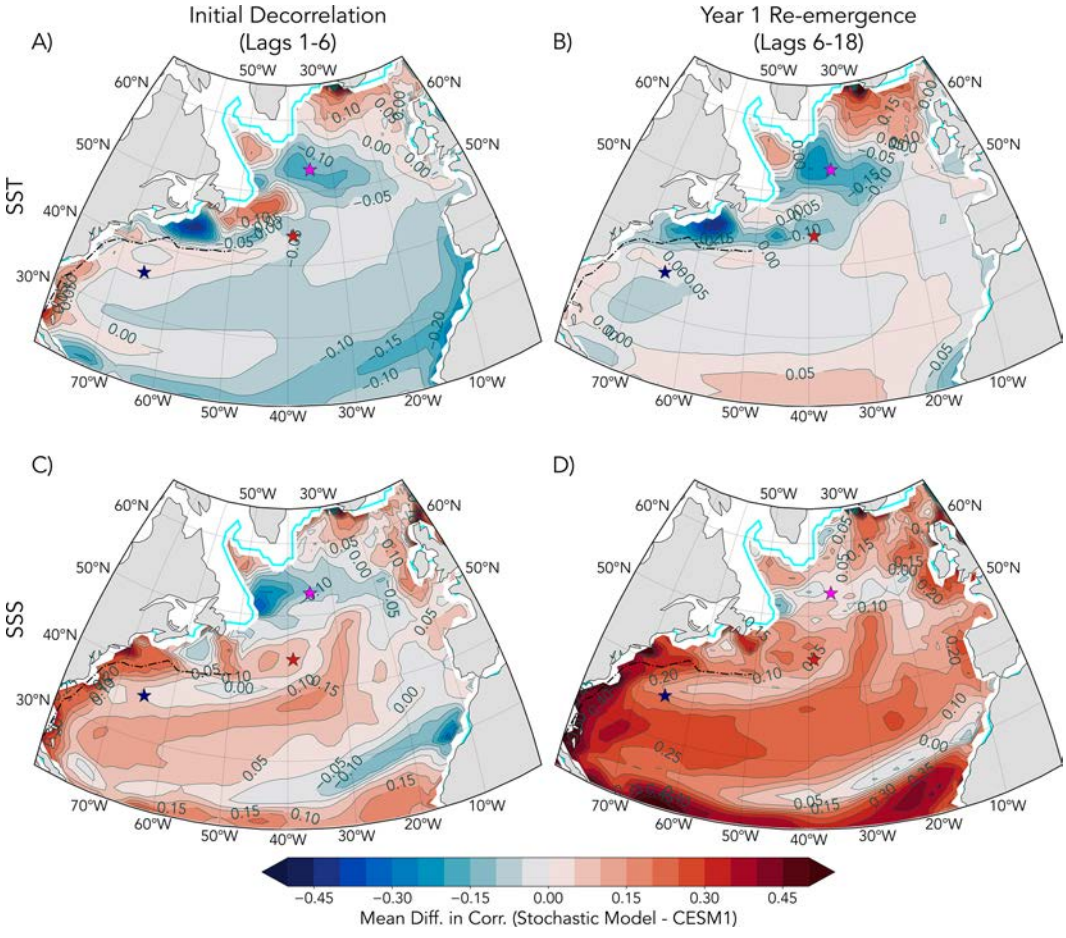

FIG. 12. Mean difference in AC (stochastic model minus CESM1) over two different lag ranges for the wintertime AC function: the (left) initial decorrelation (lags 1–6 months) and (right) year 1 reemergence (lags 6–18) for (a),(b) SST and (c),(d) SSS.

Figs. 12b,d). The spatial pattern of differences remains similar at longer lags (not shown).

Stochastic model SSTs are comparable to CESM1 over much of the subtropics, with only slight underestimates in both persistence (Figs. 12a,b) and σ(SST), hinting at the AMV horseshoe pattern (Fig. 13b). Larger underestimates south of Newfoundland and near IRM suggest that the missing processes should enhance both σ_{SST} and long-term persistence there.

Locations with overestimated SST persistence also exhibit too high σ(SST). An example is the northeastern subpolar gyre, where deep wintertime mixed layers suggest a potential role for mixed-layer variability [Eq. (4), term D]. During spring and summer, SST is too persistent along the Gulf Stream (Fig. 12a), suggesting that missing advection (terms B–C) or mixing (term G) should provide a short-term damping of SST, particularly considering strong mean gradients and currents in this region (Fig. 1a).

Similar relationships exist between SSS persistence and σ over regions with strong mean advection (Figs. 12c,d and 13d). SSS is too persistent nearly everywhere, especially along the Gulf Stream, NAC, and the subpolar gyre boundary. Overestimated σ also occurs along these advective pathways, emphasizing that missing horizontal circulation and mixing should reduce both SSS variability and persistence. Similar to SST, underestimates of initial SSS persistence and σ are found in the western subpolar gyre and south of Newfoundland. Unlike SST, SSS is overly persistent and variable in the subtropics despite weaker mean advection. Local diffusivity at the mixed-layer base (term H) could provide a source of damping (Kolodziejczyk and Gaillard 2013).

Two common threads emerge from regional differences in persistence and σ. The first concerns underestimates south of Newfoundland and in the western-central subpolar gyre where MLD variability is large, suggesting that the responsible processes should involve these properties. The second concerns large overestimates of persistence and σ relative to CESM1 in regions of strong mean advection such as the Gulf Stream and subpolar gyre boundary. Importantly, persistence and σ overestimates are larger for SSS, suggesting that the processes involved should damp SSS more strongly than SST.

We thus qualitatively investigate potential contributions of two missing processes corresponding to each thread: 1) local

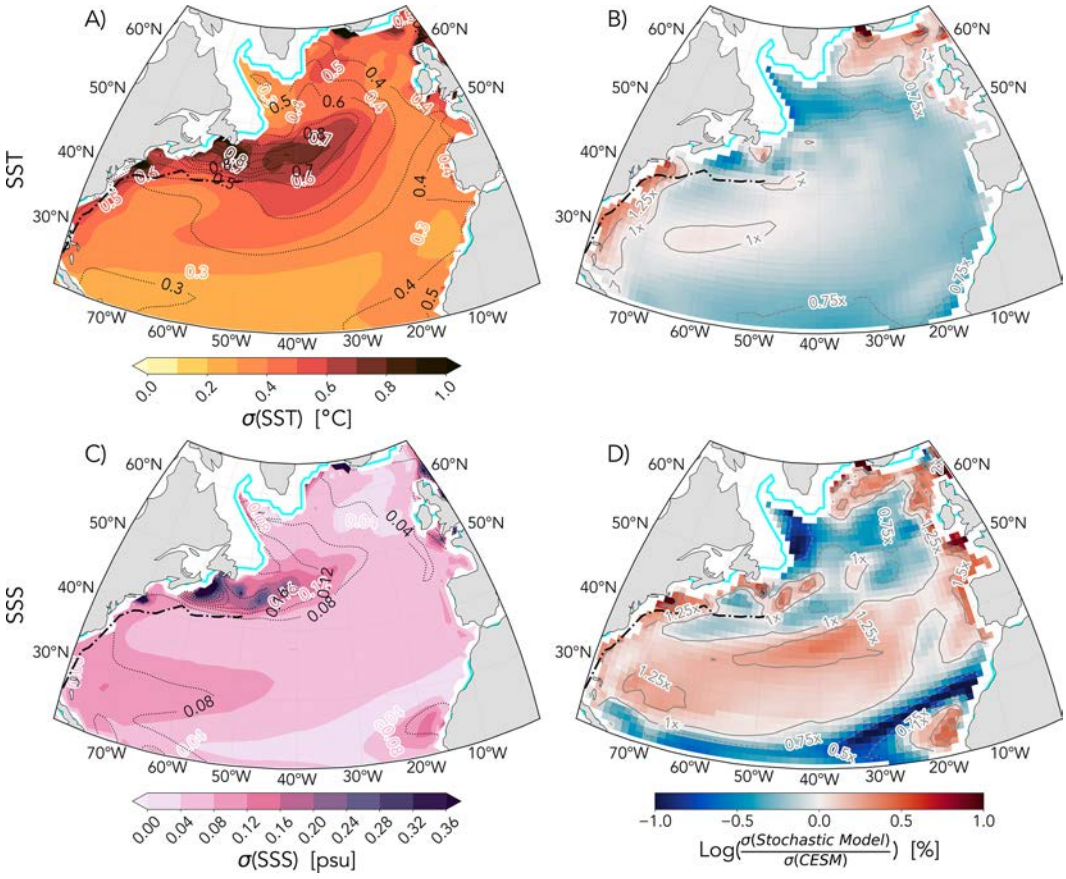

FIG. 13. The standard deviation of (a) SST and (c) SSS for the stochastic model (colors) and CESM1 (contours), computed separately for each month and then averaged for all months. The ratio (stochastic model to CESM1; %) for each variable is shown in (b) and (d). Blue (red) indicates that the stochastic model underestimates (overestimates) total variability at interannual and longer time scales relative to CESM1.

MLD variability (term D) and 2) geostrophic advection in the mixed layer (components of terms B–C). Each term is computed from CESM1 output, and the amplitude is assessed by taking the standard deviation separately for each month (σ_{Int}). We then discuss potential contributions from mesoscale processes and vertical diffusion.

b. MLD variability

A major simplification of the stochastic model is the assumption of a fixed MLD seasonal cycle. Year-to-year MLD variations affect the variability of SST and SSS in several ways, such as by (i) changing thickness of the mixed layer, thus changing the system's inertia or memory (Elsberry and Garwood 1978; Li et al. 2020) and (ii) altering the entrainment velocity during the fall months when the mixed layer deepens (Alexander and Penland 1996). Previous studies investigated contributions of MLD variations to SST variability (Alexander and Penland 1996; Li et al. 2020; Senapati et al. 2024), but fewer have explored its impact on SSS variability in the context of multidecadal North Atlantic climate. In-depth investigation of the entrainment velocity anomalies, including those associated with Ekman pumping, would require a more complex numerical mixed-layer model. We thus only focus on (i), the direct modulation due to MLD anomalies.

MLD variability plays an especially important role for SST during the spring and summer, when MLD anomalies (h') are of comparable magnitude to the mean MLD $\overline{h}$ and are driven by variations in mechanical mixing (Alexander and Penland 1996; Senapati et al. 2024). In CESM1, interannual variability of MLD anomalies is large in the Labrador Sea and eastern subtropical Atlantic, where $\sigma_{\text{Int}}(h')$ is 25%–60% of the mean MLD (Fig. 14a), suggesting that mechanism (i) may be important there. To explicitly investigate the impact of (i), we compute term D [Eq. (4)] from CESM1, using a forward difference of the mean climatological $\overline{\text{SSS}}$ or $\overline{\text{SST}}$ to calculate $\partial\overline{S}/\partial t$ and $\partial\overline{T}/\partial t$.

Over the Labrador Sea and south of Newfoundland, the amplitude of term D [σ_{Int} (term D), Fig. 14b] is comparable to the stochastic forcing applied to SST over much of the extratropics (>0.25°C month^{-1}, Figs. 4k,l). The σ_{Int} is also comparable to amplitudes of evaporation–precipitation forcing for SSS as well (>0.015 psu month^{-1}; Fig. 14c). The co-occurrence of strong σ_{Int} (term D) with underestimated SST and SSS variability suggests that this process could significantly contribute

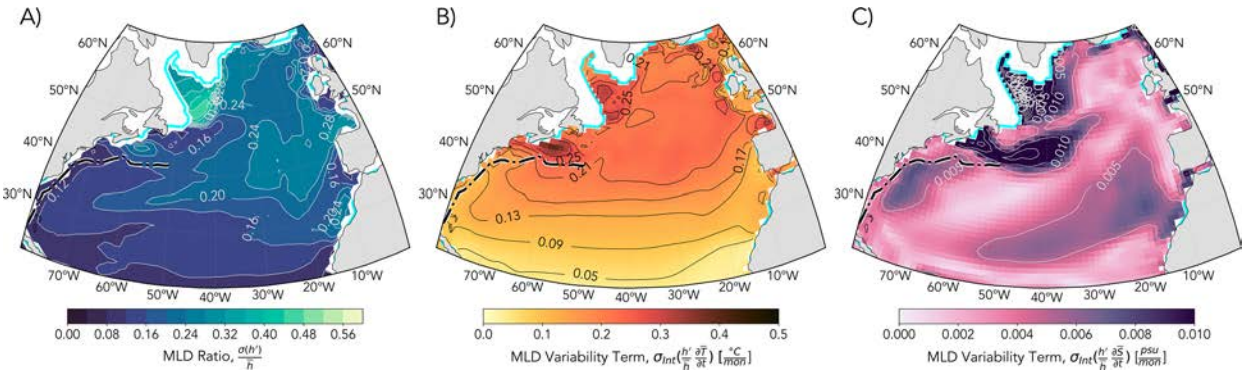

FIG. 14. (a) Mean ratio of standard deviation for monthly MLD anomalies over mean monthly MLD $[\sigma(h')/\overline{h}]$; (b) standard deviation for term D for SST $\{\sigma[(h'/\overline{h})(\partial\overline{T}/\partial t)]$; °C month$^{-1}\}$; (c) as in (b), but for SSS $\{\sigma[(h'/\overline{h})(\partial\overline{S}/\partial t)]$; psu month$^{-1}\}$. All terms are computed at each location and month before averaging across all months.

to the missing variability of the stochastic model in these regions.

We note that the use of monthly values in our calculations underestimates the contributions of MLD variability; preliminary calculations using daily output at the three illustrative locations from a CESM1 ensemble member indicate that the σ (MLD) within each month can be up to 2.5 times larger than at monthly resolution, particularly in the late spring to summer months (not shown). However, a quantitative estimate of the net impact of MLD variability on SST and SSS would require considering its influence on entrainment variability [terms E–F in Eq. (4)], which is beyond the scope of this paper.

c. *Geostrophic advection*

To estimate potential contributions of geostrophic advection to SST and SSS variability [components of terms B–C, Eq. (4)], we compute this term using sea surface height to estimate surface geostrophic currents. This calculation likely overestimates the advection effect as vertical shear in geostrophic velocities within the mixed layer is neglected, but it provides an upper bound for the contribution of geostrophic transport. We focus on the total geostrophic transport term ($u_{geo} \cdot \nabla T$ and $u_{geo} \cdot \nabla S$) since the spatial pattern and amplitude are similar between anomalous and mean geostrophic advection.

The geostrophic transport term is maximum over the Gulf Stream and NAC region, where currents are strong (Fig. 15). This term is up to an order of magnitude larger than precipitation and evaporation forcing for SSS (Fig. 15b vs Figs. 4m,n) and up to 2–3 times larger than stochastic heat flux forcing in SST (Fig. 15a vs Fig. 4k), suggesting that geostrophic advection should more strongly impact SSS than SST. In contrast, contributions from geostrophic advection are minimal elsewhere, in particular at SAR, where the stochastic model reproduces the level of variance in CESM1 (Figs. 8a,d).

Our results suggest that the missing terms should damp low-frequency SSS variance but have less impact on SST variance. While vertical diffusivity at the mixed-layer base is one potential source of damping due to its larger role in the salt budget (Kolodziejczyk and Gaillard 2013), the

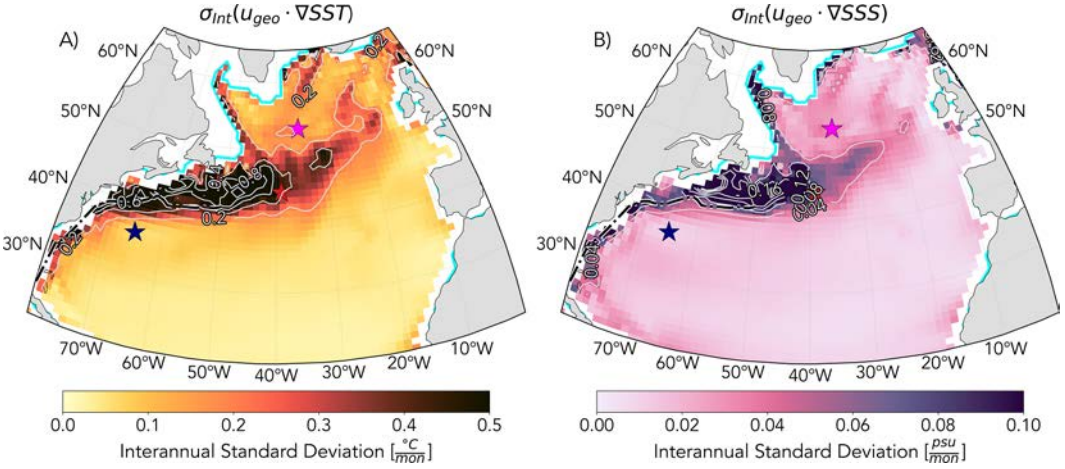

FIG. 15. Standard deviation of the geostrophic advection term for (a) SST (°C month^{-1}) and (b) SSS (psu month^{-1}), computed separately for each month and then averaged. The illustrative locations are shown for reference.

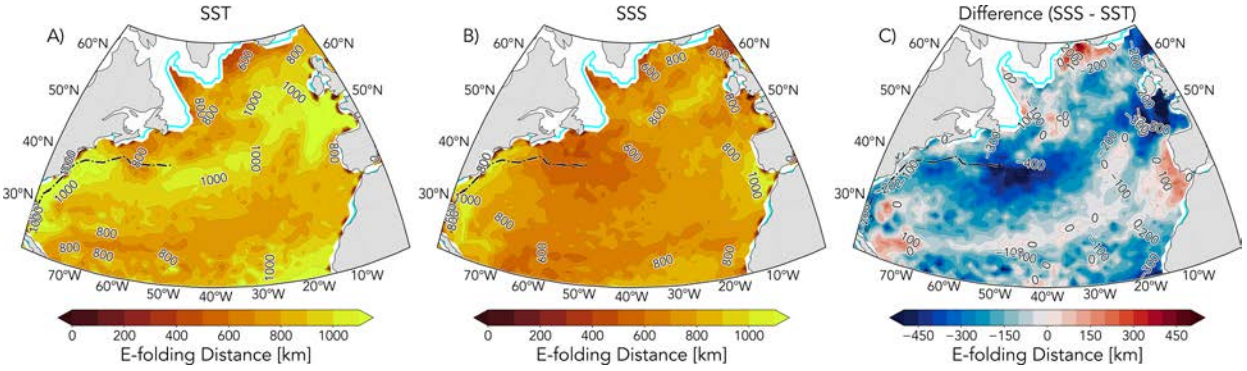

FIG. 16. Spatial *e*-folding scale (km) for (a) SST and (b) SSS anomalies, and (c) their difference, where blue (red) indicates locations where the *e*-folding scale is larger (smaller) for SST.

missing advection could also impact SST and SSS differently. Previous work by Frankignoul and Reynolds (1983) examined the role of advection for SST variance in a simple stochastic model without seasonal variation and entrainment. In wavenumber–frequency space, their analysis yielded the relationship:

$$F_{\mathrm{TT}}(\omega) \approx \int dk \frac{F_{\mathrm{NN}}(k, 0)}{(\omega - k \cdot \overline{u})^2 + \lambda^2}, \tag{19}$$

where F_{TT} is the power spectrum of SST anomalies, F_{NN} that of white noise atmospheric forcing, k is the wavenumber, ω is the frequency, $\overline{u}$ is the mean advection, and λ is the net damping. While advection should not affect high-frequency SST behavior ($\omega \gg 1$), it could significantly reduce the power at low frequencies, depending on the relative strength of $(k\overline{u})^2$ and λ^2. The same holds for SSS.

Since the net damping for SSS is 60%–80% smaller than for SST due to the absence of direct surface flux damping (not shown), the SSS power spectra should be more reduced by advection effects. Intuitively, since SSS anomalies are very persistent, advection may control their apparent damping by carrying them away, while SST anomalies may already be damped by the heat flux feedback. Following this hypothesis, we expect larger overestimates for low-frequency SSS in regions with either large advection or small-scale SSS anomalies.

Pointwise estimates of spatial decorrelation scale are obtained by fitting an exponential function to the correlation versus distance of SST and SSS anomalies. These estimates reveal that SSS anomalies generally have shorter *e*-folding distances throughout the North Atlantic (i.e., $k_{\mathrm{SSS}} > k_{\mathrm{SST}}$), enhancing their sensitivity to advection (Fig. 16). This suggests that geostrophic advection could act as a stronger damping for SSS than SST, perhaps explaining in part the most glaring stochastic model–CESM1 discrepancies, though further process studies are needed to quantify its impact.

d. Mesoscale processes and vertical diffusion

Vertical diffusion at the mixed-layer base may provide a potential source of damping to SSS with minor impacts on SST. Salt budget calculations by Kolodziejczyk and Gaillard (2013) over the subtropical southeast Pacific have identified this term as a potential strong contributor, particularly during winter months. In the subtropical Atlantic, large vertical salinity gradients in late winter and a strong density-compensating layer at the mixed-layer base lead to injection of anomalies to the ocean interior, translating to strong interannual variability within subducted isopycnal layers (Yeager and Large 2004, 2007). This variable pulse of late-winter signals and interactions with subducted subsurface waters could lead to an additional source of SSS damping not included in the stochastic model.

The coarse resolution (1°) of CESM1 presents a challenge for understanding contributions of ocean mesoscale processes, likely leading to an underestimate in the role of ocean dynamics. Multiple studies have noted increased SST and SSS variance in high-resolution (HR) simulations compared to their low-resolution counterparts with parameterized mesoscale processes due to contribution of mesoscale processes to intrinsic oceanic forcing (Kirtman et al. 2012; Smirnov et al. 2014; Bishop et al. 2017; Small et al. 2020; Siqueira et al. 2024; Laurindo et al. 2024). Mesoscale variability would likely widen the underestimation of SST variance by the stochastic model, leaving a greater role for missing ocean processes in driving variability. Furthermore, increased gradients from improvements in representation of SST/SSS gradients, fronts, and filaments can further enhance the role of nonlocal processes, providing additional sources of ocean damping that are critically missing from the stochastic model's representation of SSS persistence (Bishop et al. 2017; Putrasahan et al. 2017; Sun and Wu 2022). Contributions of mesoscale processes could be explored within the stochastic model framework using bulk oceanic forcing and damping terms parameterized based on HR output, but finer separation into specific processes remains a challenge (Patrizio and Thompson 2022; Laurindo et al. 2022, 2024; Siqueira et al. 2024). Future work investigating the SST–SSS relationship and its sensitivity to resolution could thus provide further insights into the variability and predictability of the North Atlantic climate.

6. Summary

While studies on interannual-to-multidecadal climate variability over the North Atlantic often focus on SST, less attention has been given to SSS variability and the contributions of

local, vertical processes. Understanding of SSS variability is complicated by limited observational records, particularly in the subpolar Atlantic, where deep wintertime MLDs portend the strong influence of vertical processes for long-term variability. Using 3612 years of monthly output from the CESM1 Large Ensemble, we investigate the drivers of SSS variability and its relationship to SST.

Wintertime SST and SSS in CESM1 exhibit strong recurring signals in regions south of the Gulf Stream and within the central subpolar gyre (Figs. 2a,b). These patterns of reemergence are strikingly reproduced by a simple stochastic model without horizontal advection, suggesting the power of local, vertical processes in capturing SST and SSS persistence (Figs. 2c,d).

We investigate contributions of subsurface damping and SST–evaporation feedback by successively including each process in a hierarchy of stochastic models. Damping of subsurface anomalies enables successful simulation of SST behavior over most locations and is particularly important for capturing correct seasonal differences in persistence (Figs. 7–9). Subsurface damping is essential to simulate SSS variability, though there remain strong overestimates of SSS persistence and variance, indicating that missing damping processes are more important for this variable (Figs. 12 and 13). The impact of SST–evaporation feedback on SSS is smaller but notable in locations with large positive SST–SSS correlation such as in the NAC (Fig. 10).

Overall, the local dynamics included in the stochastic model can explain many spatiotemporal signatures of North Atlantic SST and SSS variability but cannot capture their magnitude (Fig. 11). This reinforces the findings by Liu et al. (2023) that processes beyond local atmospheric forcing, entrainment, and anomalous Ekman forcing are needed to correctly represent the amplitude of AMV. Interannual MLD is a potential candidate for some of the missing variance, particularly in the western subpolar gyre and south of Newfoundland (Fig. 14).

Critically, our results highlight how ocean processes may not have the same impact on SST and SSS. The stochastic model–CESM1 discrepancies suggest that the missing processes should provide a strong damping source to the overestimated SSS with less impact on SST. Potential solutions involve differences in spatial scales between both variables (Fig. 16), differences in the amplitude of geostrophic advection (Fig. 15), and vertical diffusion at the mixed-layer base. Analysis of high-resolution simulations or developments in the stochastic model, particularly considering neglected anomalous vertical velocities, could clarify the damping or forcing roles of the missing terms from the stochastic model framework, shedding further light on the drivers of large-scale salinity and temperature variations.

Acknowledgments. The authors gratefully acknowledge support from the National Science Foundation Climate and Large-scale Dynamics Program (AGS-2055236) and the Physical Oceanography Program (OCE-2219436). GL is supported by the Department of Defense (DoD) through the National Defense Science and Engineering Graduate (NDSEG) Fellowship Program. The authors thank the editor, Yuko Okumura, Martha Buckley, and two anonymous reviewers for their insightful comments and suggestions, which strengthened this study.

Data availability statement. All data used for this work are available online. CESM1-LE simulations are available through the NCAR Climate Data Gateway (https://www.cesm.ucar.edu/projects/community-projects/LENS/data-sets.html).

APPENDIX A

Parameters and Units

Table A1 shows the parameters and corresponding symbols and units.

TABLE A1. Variables used in the stochastic SST and SSS equations, with full names and units.

Parameter	Name	Units
T', SST	Anomalous SST	°C
S', SST	Anomalous SSS	psu
T'_d, S'_d	Detrained temperature/salinity below mixed layer	°C, psu
λ^N, λ^L	Net and latent heat flux feedback	W m^{-2} °C^{-1}
λ^d_T, λ^d_S	Subsurface SST and SSS damping	Unitless
λ^e	SST–evaporation feedback on SSS	psu °C^{-1} s^{-1}
τ^d_T, τ^d_S	Subsurface damping time scale	months
τ^N	Net heat flux damping time scale	months
Q'_N, Q'_L	Net and latent heat flux	W m^{-2}
F'_N, F'_L	Stochastic net and latent heat flux forcing	W m^{-2}
P'	Precipitation forcing	psu s^{-1}
$\overline{S}$	Mean salinity	psu
h	MLD	m
B	Bowen ratio	Unitless
u'_{ek}	Anomalous Ekman current	m s^{-1}
$Q'_{\mathrm{ek},T}$, $Q'_{\mathrm{ek},S}$	Anomalous SST and SSS Ekman forcing	W m^{-2}
u'_{geo}	Anomalous geostrophic current	m s^{-1}
τ	Time lag	months
Δt	Integration step	months
τ_x, τ_y	Zonal/meridional wind stress	N m^{-2}
ρ	Density of seawater	kg m^{-3}
$\mathbb{R}$	EOF forcing pattern	°C month^{-1}, psu month^{-1}
$\mathbb{C}$	Correction factor	°C month^{-1}, psu month^{-1}
N	White noise time series	Unitless

APPENDIX B

Integrating the Stochastic Salinity Model

We describe the discretization procedure for the stochastic salinity model, beginning from Eq. (10). First, group all terms dependent on S' to the left side of the equation:

$$e^{-\lambda t}\frac{\partial}{\partial t}(e^{\lambda t}S') = \lambda^e T' + \frac{\overline{S}}{\rho h}\left(-\frac{F'_L}{L} - P'\right) + \frac{\overline{w_e}}{h}S'_d + Q'_{\mathrm{ek},S}, \tag{B1}$$

where the total damping (λ) consists of only the entrainment damping ($\overline{w_e}/h$), which is constant over the integration step. Multiplying Eq. (B1) by $e^{\lambda t}$ and integrating from t to $t + \Delta t$ yields

$$S'(t+\Delta t) = e^{-\lambda\Delta t}S'(t) + \left\{\frac{\overline{w_e}}{h}S'_d + \left[\frac{\overline{S}}{\rho h}\left(-\frac{F'_L}{L} - P'\right)\right] + Q'_{\mathrm{ek},S} + \lambda^e T'\right\}\int_t^{t+\Delta t} e^{-\lambda(t+\Delta t-t')}dt', \tag{B2}$$

where the forcing terms (within the curly brackets) are assumed to be constant over the monthly time step. The integral in Eq. (B2) is simplified by substituting $\tau = t' - t$ and integrating over the monthly step between 0 to Δt, yielding an integration factor:

$$\int_t^{t+\Delta t} e^{-\lambda(t+\Delta t-t')}dt' = \int_0^{\Delta t} e^{\lambda(\tau-\Delta t)}d\tau = \left(\frac{1-e^{-\lambda\Delta t}}{\lambda}\right). \tag{B3}$$

The monthly averaged entrainment velocity can be further rewritten as

$$\frac{\overline{w_e}}{h} = \frac{1}{\Delta t}\int_t^{t+\Delta t}\left(\frac{1}{h}\frac{\partial h}{\partial t'}\right)dt' = \frac{1}{\Delta t}\ln\left[\frac{h(t+\Delta t)}{h(t)}\right], \tag{B4}$$

where $h(t)$ and $h(t + \Delta t)$ refer to climatological mixed-layer depths for the current and following month. Similarly, the salinity below the thermocline S'_d is given by

$$\overline{S'_d} = \frac{S'_d(t) + S'_d(t+\Delta t)}{2}, \tag{B5}$$

where S'_d is calculated considering the subsurface damping (λ^d_S) of anomalies [Eq. (17)]. Substituting Eqs. (B3)–(B5) into Eq. (B2), the discretized form of the stochastic model [Eq. (13)] is recovered.

APPENDIX C

Estimating the Stochastic Forcing

The procedure for estimating the forcing can be broken into four steps, performed separately for each calendar month m on all CESM1 ensemble members together:

1) Retrieve the principal component time series of the stochastic component of the net heat flux [F'_N, Eq. (12)] over the North Atlantic basin.
2) Retain enough modes (k) to explain 90% of the variance of each month to focus on large-scale forcing. This ranges between 15 modes in the winter to 79 modes in the summer months.
3) Regress the target forcing term (e.g., Ekman forcing, precipitation) onto the standardized principal component time series to obtain corresponding forcing patterns [$\mathbb{P}(x, y, k, m)$]. Figure 4 shows the winter forcing patterns of mode one (A–E), two (F–J), and the sum of the k retained modes (K–O).
4) Compute and add a correction factor [$\mathbb{C}(x, y, m)$] at each point and month by subtracting the total variance represented by $\mathbb{P}$ from the variance of the original term (e.g., Ekman forcing, precipitation). This procedure ensures that the monthly variances are preserved at each grid point and the signs are coherent across different terms, preserving the large-scale spatial structure of the forcing. This EOF-based forcing largely captures the variance but requires larger corrections for precipitation and Ekman forcing near the coastlines and Gulf Stream (Figs. 4p–t).

For example, the stochastic latent heat flux forcing (F'_L) is given by

$$F'_L(x, y, t) = \sum_{n=1}^{k}[\mathbb{P}(x, y, n, m)N(n, t)] + \mathbb{C}(x, y, m)N(t), \tag{C1}$$

where $\mathbb{P}$ are the regression patterns of stochastic latent heat flux, N is a set of white noise time series with unit variance, and $\mathbb{C}$ is the additive correction factor. All other forcing components are computed in the same way. Note that while each EOF mode and correction factor receives its own white noise time series, the same set of k white noise time series is applied to all other forcing components. This ensures that the signs are coherent across the different terms, preserving the large-scale spatial structure of the forcing.

REFERENCES

Alexander, M. A., and C. Deser, 1995: A mechanism for the recurrence of wintertime midlatitude SST anomalies. *J. Phys. Oceanogr.*, **25**, 122–137, https://doi.org/10.1175/1520-0485(1995)025<0122:AMFTRO>2.0.CO;2.

——, and C. Penland, 1996: Variability in a mixed layer ocean model driven by stochastic atmospheric forcing. *J. Climate*, **9**, 2424–2442, https://doi.org/10.1175/1520-0442(1996)009<2424:VIAMLO>2.0.CO;2.

——, and J. D. Scott, 2008: The role of Ekman ocean heat transport in the Northern Hemisphere response to ENSO. *J. Climate*, **21**, 5688–5707, https://doi.org/10.1175/2008JCLI2382.1.

Bishop, S. P., R. J. Small, F. O. Bryan, and R. A. Tomas, 2017: Scale dependence of midlatitude air–sea interaction. *J. Climate*, **30**, 8207–8221, https://doi.org/10.1175/JCLI-D-17-0159.1.

Bryan, F., and S. Bachman, 2015: Isohaline salinity budget of the North Atlantic salinity maximum. *J. Phys. Oceanogr.*, **45**, 724–736, https://doi.org/10.1175/JPO-D-14-0172.1.

Buckley, M. W., R. M. Ponte, G. Forget, and P. Heimbach, 2014: Low-frequency SST and upper-ocean heat content variability in the North Atlantic. *J. Climate*, **27**, 4996–5018, https://doi.org/10.1175/JCLI-D-13-00316.1.

——, ——, ——, and ——, 2015: Determining the origins of advective heat transport convergence variability in the North Atlantic. *J. Climate*, **28**, 3943–3956, https://doi.org/10.1175/JCLI-D-14-00579.1.

——, T. DelSole, M. S. Lozier, and L. Li, 2019: Predictability of North Atlantic sea surface temperature and upper-ocean heat content. *J. Climate*, **32**, 3005–3023, https://doi.org/10.1175/JCLI-D-18-0509.1.

Byju, P., D. Dommenget, and M. A. Alexander, 2018: Widespread reemergence of sea surface temperature anomalies in the global oceans, including tropical regions forced by reemerging winds. *Geophys. Res. Lett.*, **45**, 7683–7691, https://doi.org/10.1029/2018GL079137.

Danabasoglu, G., S. C. Bates, B. P. Briegleb, S. R. Jayne, M. Jochum, W. G. Large, S. Peacock, and S. G. Yeager, 2012: The CCSM4 ocean component. *J. Climate*, **25**, 1361–1389, https://doi.org/10.1175/JCLI-D-11-00091.1.

de Coëtlogon, G., and C. Frankignoul, 2003: The persistence of winter sea surface temperature in the North Atlantic. *J. Climate*, **16**, 1364–1377, https://doi.org/10.1175/1520-0442-16.9.1364.

Deser, C., M. A. Alexander, and M. S. Timlin, 2003: Understanding the persistence of sea surface temperature anomalies in midlatitudes. *J. Climate*, **16**, 57–72, https://doi.org/10.1175/1520-0442(2003)016<0057:UTPOSS>2.0.CO;2.

——, and Coauthors, 2020: Insights from earth system model initial-condition large ensembles and future prospects. *Nat. Climate Change*, **10**, 277–286, https://doi.org/10.1038/s41558-020-0731-2.

Elsberry, R. L., and R. W. Garwood Jr., 1978: Sea-surface temperature anomaly generation in relation to atmospheric storms. *Bull. Amer. Meteor. Soc.*, **59**, 786–789, https://doi.org/10.1175/1520-0477(1978)059<0786:SSTAGI>2.0.CO;2.

Frankignoul, C., 1985: Sea surface temperature anomalies, planetary waves, and air-sea feedback in the middle latitudes. *Rev. Geophys.*, **23**, 357–390, https://doi.org/10.1029/RG023i004p00357.

——, and K. Hasselmann, 1977: Stochastic climate models, part II application to sea-surface temperature anomalies and thermocline variability. *Tellus*, **29A**, 289–305, https://doi.org/10.3402/tellusa.v29i4.11362.

——, and R. W. Reynolds, 1983: Testing a dynamical model for mid-latitude sea surface temperature anomalies. *J. Phys. Oceanogr.*, **13**, 1131–1145, https://doi.org/10.1175/1520-0485(1983)013<1131:TADMFM>2.0.CO;2.

——, and E. Kestenare, 2002: The surface heat flux feedback. Part I: Estimates from observations in the Atlantic and the North Pacific. *Climate Dyn.*, **19**, 633–647, https://doi.org/10.1007/s00382-002-0252-x.

——, A. Czaja, and B. L'Heveder, 1998: Air–sea feedback in the North Atlantic and surface boundary conditions for ocean models. *J. Climate*, **11**, 2310–2324, https://doi.org/10.1175/1520-0442(1998)011<2310:ASFITN>2.0.CO;2.

——, J. Deshayes, and R. Curry, 2009: The role of salinity in the decadal variability of the North Atlantic meridional overturning circulation. *Climate Dyn.*, **33**, 777–793, https://doi.org/10.1007/s00382-008-0523-2.

——, E. Kestenare, and G. Reverdin, 2021: Sea surface salinity reemergence in an updated North Atlantic in situ salinity dataset. *J. Climate*, **34**, 9007–9023, https://doi.org/10.1175/JCLI-D-20-0840.1.

Friedman, A. R., G. Reverdin, M. Khodri, and G. Gastineau, 2017: A new record of Atlantic sea surface salinity from 1896 to 2013 reveals the signatures of climate variability and long-term trends. *Geophys. Res. Lett.*, **44**, 1866–1876, https://doi.org/10.1002/2017GL072582.

Gozdz, O., M. W. Buckley, and T. DelSole, 2024: The impact of interactive ocean dynamics on Atlantic sea surface temperature variability. *J. Climate*, **37**, 2937–2964, https://doi.org/10.1175/JCLI-D-23-0609.1.

Haarsma, R. J., E. J. D. Campos, W. Hazeleger, C. Severijns, A. R. Piola, and F. Molteni, 2005: Dominant modes of variability in the South Atlantic: A study with a hierarchy of ocean–atmosphere models. *J. Climate*, **18**, 1719–1735, https://doi.org/10.1175/JCLI3370.1.

Hall, A., and S. Manabe, 1997: Can local linear stochastic theory explain sea surface temperature and salinity variability? *Climate Dyn.*, **13**, 167–180, https://doi.org/10.1007/s003820050158.

Hanawa, K., and S. Sugimoto, 2004: 'Reemergence' areas of winter sea surface temperature anomalies in the world's oceans. *Geophys. Res. Lett.*, **31**, L10303, https://doi.org/10.1029/2004GL019904.

Hasselmann, K., 1976: Stochastic climate models part I. Theory. *Tellus*, **28**, 473–485, https://doi.org/10.1111/j.2153-3490.1976.tb00696.x.

Hughes, T. M. C., and A. J. Weaver, 1996: Sea surface temperature-evaporation feedback and the ocean's thermohaline circulation. *J. Phys. Oceanogr.*, **26**, 644–654, https://doi.org/10.1175/1520-0485(1996)026<0644:SSTEFA>2.0.CO;2.

Hurrell, J. W., and C. Deser, 2010: North Atlantic climate variability: The role of the North Atlantic Oscillation. *J. Mar. Syst.*, **79**, 231–244, https://doi.org/10.1016/j.jmarsys.2009.11.002.

——, and Coauthors, 2013: The Community Earth System Model: A framework for collaborative research. *Bull. Amer. Meteor. Soc.*, **94**, 1339–1360, https://doi.org/10.1175/BAMS-D-12-00121.1.

Kay, J. E., and Coauthors, 2015: The Community Earth System Model (CESM) large ensemble project: A community resource for studying climate change in the presence of internal climate variability. *Bull. Amer. Meteor. Soc.*, **96**, 1333–1349, https://doi.org/10.1175/BAMS-D-13-00255.1.

Kirtman, B. P., and Coauthors, 2012: Impact of ocean model resolution on CCSM climate simulations. *Climate Dyn.*, **39**, 1303–1328, https://doi.org/10.1007/s00382-012-1500-3.

Kolodziejczyk, N., and F. Gaillard, 2013: Variability of the heat and salt budget in the subtropical southeastern Pacific mixed layer between 2004 and 2010: Spice injection mechanism. *J. Phys. Oceanogr.*, **43**, 1880–1898, https://doi.org/10.1175/JPO-D-13-04.1.

Laurindo, L. C., and Coauthors, 2022: Role of ocean and atmosphere variability in scale-dependent thermodynamic air-sea interactions. *J. Geophys. Res. Oceans*, **127**, e2021JC018340, https://doi.org/10.1029/2021JC018340.

——, L. Siqueira, R. J. Small, L. Thompson, and B. P. Kirtman, 2024: Quantifying the contribution of ocean advection and surface flux to the upper-ocean salinity variability resolved by climate model simulations. *Geophys. Res. Lett.*, **51**, e2023GL106354, https://doi.org/10.1029/2023GL106354.

Li, L., M. S. Lozier, and M. W. Buckley, 2020: An investigation of the ocean's role in Atlantic multidecadal variability. *J. Climate*, **33**, 3019–3035, https://doi.org/10.1175/JCLI-D-19-0236.1.

Liu, G., Y.-O. Kwon, C. Frankignoul, and J. Lu, 2023: Understanding the drivers of Atlantic multidecadal variability using a stochastic model hierarchy. *J. Climate*, **36**, 1043–1058, https://doi.org/10.1175/JCLI-D-22-0309.1.

Liu, L. L., and R. X. Huang, 2012: The global subduction/obduction rates: Their interannual and decadal variability. *J. Climate*, **25**, 1096–1115, https://doi.org/10.1175/2011JCLI4228.1.

Mignot, J., and C. Frankignoul, 2003: On the interannual variability of surface salinity in the Atlantic. *Climate Dyn.*, **20**, 555–565, https://doi.org/10.1007/s00382-002-0294-0.

——, and ——, 2004: Interannual to interdecadal variability of sea surface salinity in the Atlantic and its link to the atmosphere in a coupled model. *J. Geophys. Res.*, **109**, C04005, https://doi.org/10.1029/2003JC002005.

Msadek, R., and C. Frankignoul, 2009: Atlantic multidecadal oceanic variability and its influence on the atmosphere in

a climate model. *Climate Dyn.*, **33**, 45–62, https://doi.org/10.1007/s00382-008-0452-0.

Oltmanns, M., N. P. Holliday, J. Screen, B. I. Moat, S. A. Josey, D. G. Evans, and S. Bacon, 2024: European summer weather linked to North Atlantic freshwater anomalies in preceding years. *Wea. Climate Dyn.*, **5**, 109–132, https://doi.org/10.5194/wcd-5-109-2024.

Park, S., C. Deser, and M. A. Alexander, 2005: Estimation of the surface heat flux response to sea surface temperature anomalies over the global oceans. *J. Climate*, **18**, 4582–4599, https://doi.org/10.1175/JCLI3521.1.

——, M. A. Alexander, and C. Deser, 2006: The impact of cloud radiative feedback, remote ENSO forcing, and entrainment on the persistence of North Pacific sea surface temperature anomalies. *J. Climate*, **19**, 6243–6261, https://doi.org/10.1175/JCLI3957.1.

Patrizio, C. R., and D. W. Thompson, 2022: Understanding the role of ocean dynamics in midlatitude sea surface temperature variability using a simple stochastic climate model. *J. Climate*, **35**, 3313–3333, https://doi.org/10.1175/JCLI-D-21-0184.1.

——, P. J. Athanasiadis, C. Frankignoul, D. Iovino, S. Masina, L. Famooss Paolini, and S. Gualdi, 2023: Improved extratropical North Atlantic atmosphere–ocean variability with increasing ocean model resolution. *J. Climate*, **36**, 8403–8424, https://doi.org/10.1175/JCLI-D-23-0230.1.

Putrasahan, D. A., I. Kamenkovich, M. Le Hénaff, and B. P. Kirtman, 2017: Importance of ocean mesoscale variability for air-sea interactions in the Gulf of Mexico. *Geophys. Res. Lett.*, **44**, 6352–6362, https://doi.org/10.1002/2017GL072884.

Senapati, B., C. H. O'Reilly, and J. Robson, 2024: Pivotal role of mixed-layer depth in tropical Atlantic multidecadal variability. *Geophys. Res. Lett.*, **51**, e2024GL110057, https://doi.org/10.1029/2024GL110057.

Siqueira, L., B. P. Kirtman, L. C. Laurindo, J. T. Fasullo, and A. Hu, 2024: Quantifying the role of ocean dynamics in SST variability across GCMs and observations. *J. Climate*, **37**, 5721–5737, https://doi.org/10.1175/JCLI-D-23-0686.1.

Small, R. J., F. O. Bryan, S. P. Bishop, S. Larson, and R. A. Tomas, 2020: What drives upper-ocean temperature variability in coupled climate models and observations? *J. Climate*, **33**, 577–596, https://doi.org/10.1175/JCLI-D-19-0295.1.

Smirnov, D., M. Newman, and M. A. Alexander, 2014: Investigating the role of ocean–atmosphere coupling in the North Pacific Ocean. *J. Climate*, **27**, 592–606, https://doi.org/10.1175/JCLI-D-13-00123.1.

Spall, M. A., 1993: Variability of sea surface salinity in stochastically forced systems. *Climate Dyn.*, **8**, 151–160, https://doi.org/10.1007/BF00208094.

Sterl, A., and W. Hazeleger, 2003: Coupled variability and air-sea interaction in the South Atlantic Ocean. *Climate Dyn.*, **21**, 559–571, https://doi.org/10.1007/s00382-003-0348-y.

Sugimoto, S., and K. Hanawa, 2005: Why does reemergence of winter sea surface temperature anomalies not occur in eastern mode water areas? *Geophys. Res. Lett.*, **32**, L15608, https://doi.org/10.1029/2005GL022968.

——, and ——, 2007: Further evidence for non-reemergence of winter SST anomalies in the North Pacific eastern subtropical mode water area. *J. Oceanogr.*, **63**, 625–635, https://doi.org/10.1007/s10872-007-0055-0.

Sun, X., and R. Wu, 2022: Spatial scale dependence of the relationship between turbulent surface heat flux and SST. *Climate Dyn.*, **58**, 1127–1145, https://doi.org/10.1007/s00382-021-05957-9.

Timlin, M. S., M. A. Alexander, and C. Deser, 2002: On the reemergence of North Atlantic SST anomalies. *J. Climate*, **15**, 2707–2712, https://doi.org/10.1175/1520-0442(2002)015<2707:OTRONA>2.0.CO;2.

Yeager, S. G., and W. G. Large, 2004: Late-winter generation of spiciness on subducted isopycnals. *J. Phys. Oceanogr.*, **34**, 1528–1547, https://doi.org/10.1175/1520-0485(2004)034<1528:LGOSOS>2.0.CO;2.

——, and ——, 2007: Observational evidence of winter spice injection. *J. Phys. Oceanogr.*, **37**, 2895–2919, https://doi.org/10.1175/2007JPO3629.1.

Zhang, R., 2017: On the persistence and coherence of subpolar sea surface temperature and salinity anomalies associated with the Atlantic multidecadal variability. *Geophys. Res. Lett.*, **44**, 7865–7875, https://doi.org/10.1002/2017GL074342.

——, and G. K. Vallis, 2006: Impact of great salinity anomalies on the low-frequency variability of the North Atlantic climate. *J. Climate*, **19**, 470–482, https://doi.org/10.1175/JCLI3623.1.

——, R. Sutton, G. Danabasoglu, Y.-O. Kwon, R. Marsh, S. G. Yeager, D. E. Amrhein, and C. M. Little, 2019: A review of the role of the Atlantic meridional overturning circulation in Atlantic multidecadal variability and associated climate impacts. *Rev. Geophys.*, **57**, 316–375, https://doi.org/10.1029/2019RG000644.